Extrusion-based 3D printing of biodegradable, osteogenic, paramagnetic, and porous FeMn-akermanite bone substitutes

Putra, N. E.; Leeflang, M. A.; Klimopoulou, M.; Dong, J.; Taheri, P.; Huan, Z.; Fratila-Apachitei, L. E.; Mol, J. M.C.; Chang, J.; Zhou, J.

DOI
10.1016/j.actbio.2023.03.033

Publication date
2023

Document Version
Final published version

Published in
Acta Biomaterialia

Citation (APA)
Putra, N. E., Leeflang, M. A., Klimopoulou, M., Dong, J., Taheri, P., Huan, Z., Fratila-Apachitei, L. E., Mol, J. M. C., Chang, J., Zhou, J., & Zadpoor, A. A. (2023). Extrusion-based 3D printing of biodegradable, osteogenic, paramagnetic, and porous FeMn-akermanite bone substitutes. *Acta Biomaterialia*, *162*, 182-198. https://doi.org/10.1016/j.actbio.2023.03.033

Acta Biomaterialia 162 (2023) 182–198

Contents lists available at ScienceDirect

Acta Biomaterialia

journal homepage: www.elsevier.com/locate/actbio

Full length article

Extrusion-based 3D printing of biodegradable, osteogenic, paramagnetic, and porous FeMn-akermanite bone substitutes

N.E. Putra[a,*], M.A. Leeflang[a], M. Klimopoulou[a], J. Dong[a], P. Taheri[b], Z. Huan[c], L.E. Fratila-Apachitei[a], J.M.C. Mol[b], J. Chang[c], J. Zhou[a], A.A. Zadpoor[a]

[a] Department of Biomechanical Engineering, Faculty of Mechanical, Maritime, and Materials Engineering, Delft University of Technology, Mekelweg 2, Delft 2628 CD, The Netherlands
[b] Department of Materials Science and Engineering, Faculty of Mechanical, Maritime, and Materials Engineering, Delft University of Technology, Mekelweg 2, Delft 2628 CD, The Netherlands
[c] Shanghai Institute of Ceramics, Chinese Academy of Sciences, 1295 Dingxi Road, Shanghai 200050, China

ARTICLE INFO

Article history:
Received 30 January 2023
Revised 13 March 2023
Accepted 21 March 2023
Available online 25 March 2023

Keywords:
Extrusion-based 3D printing
Biodegradable
Iron-manganese
Akermanite
Bone
Scaffold

ABSTRACT

The development of biodegradable Fe-based bone implants has rapidly progressed in recent years. Most of the challenges encountered in developing such implants have been tackled individually or in combination using additive manufacturing technologies. Yet not all the challenges have been overcome. Herein, we present porous FeMn-akermanite composite scaffolds fabricated by extrusion-based 3D printing to address the unmet clinical needs associated with Fe-based biomaterials for bone regeneration, including low biodegradation rate, MRI-incompatibility, mechanical properties, and limited bioactivity. In this research, we developed inks containing Fe, 35 wt% Mn, and 20 or 30 vol% akermanite powder mixtures. 3D printing was optimized together with the debinding and sintering steps to obtain scaffolds with interconnected porosity of 69%. The Fe-matrix in the composites contained the γ-FeMn phase as well as nesosilicate phases. The former made the composites paramagnetic and, thus, MRI-friendly. The *in vitro* biodegradation rates of the composites with 20 and 30 vol% akermanite were respectively 0.24 and 0.27 mm/y, falling within the ideal range of biodegradation rates for bone substitution. The yield strengths of the porous composites stayed within the range of the values of the trabecular bone, despite *in vitro* biodegradation for 28 d. All the composite scaffolds favored the adhesion, proliferation, and osteogenic differentiation of preosteoblasts, as revealed by Runx2 assay. Moreover, osteopontin was detected in the extracellular matrix of cells on the scaffolds. Altogether, these results demonstrate the remarkable potential of these composites in fulfilling the requirements of porous biodegradable bone substitutes, motivating future *in vivo* research.

Statement of significance

We developed FeMn-akermanite composite scaffolds by taking advantage of the multi-material capacity of extrusion-based 3D printing. Our results demonstrated that the FeMn-akermanite scaffolds showed an exceptional performance in fulfilling all the requirements for bone substitution *in vitro, i.e.*, a sufficient biodegradation rate, having mechanical properties in the range of trabecular bone even after 4 weeks biodegradation, paramagnetic, cytocompatible and most importantly osteogenic. Our results encourage further research on Fe-based bone implants in *in vivo*.

1. Introduction

In recent years, remarkable progress has been made in the development of biodegradable Fe-based metals to assist in the regeneration of critical-size bony defects. In particular, researchers have tried to address some key challenges and find viable solutions to speed up the clinical adoption of such metals [1]. The first challenge concerns the slow degradation rate of pure Fe *in vivo* [2]. To improve their biodegradation profile, Fe implants have been recently designed to possess geometrically ordered porous structures, which are then realized through additive

* Corresponding author.
E-mail address: n.e.putra@tudelft.nl (N.E. Putra).

https://doi.org/10.1016/j.actbio.2023.03.033

manufacturing (AM) [3]. The resulting hierarchical porous Fe structures have, indeed, exhibited enhanced rates of biodegradation *in vitro* [4]. The second challenge concerns the inherent ferromagnetic behavior of Fe, which hinders its use in patients who may need magnetic resonance imaging (MRI) during their treatments. Alloying Fe with >28 wt% Mn has been shown to make Fe antiferromagnetic [5], thereby removing a critically important barrier to potential clinical adoption of Fe-based implants, while also increasing the biodegradation rate of Fe [6]. In addition, the mechanical properties of FeMn alloys have been shown to be tunable by varying the porosity, pore shape, and pore sizes so as to match the mechanical properties of the trabecular bone [7,8] as well as those of the cortical bone [9–11].

Despite all these developments, the biocompatibility of FeMn alloys for bone implants remains limited, potentially hindering the progress of the bone tissue regeneration. Porosity has been generally found to dictate the biodegradation profile and, thus, the biological response of Fe-based materials. For porosities < 40 vol%, several studies have found FeMn alloys to be cytocompatible with cell types such as mouse preosteoblasts MC3T3-E1 [12–14], mouse fibroblasts (3T3 [15], L929 [16]), and mouse bone marrow stromal cells (BMSCs) [7]. FeMn alloys with higher porosities (*e.g.*, 60 vol% [7] and 69 vol% [17]), however, have presented *in vitro* cytotoxicity against mouse BMSCs [7] and preosteoblasts MC3T3-E1 [17]. That said, one study has reported *in vitro* cytocompatibility of 85 vol% porous FeMn alloy structures for MC3T3-E1 cells [8]. The picture regarding the biological performance of porous FeMn alloys is incomplete because most of the findings regarding their *in vitro* cytocompatibility is based on short-term *in vitro* tests (*i.e.*, up to 7 days), while their osteogenic potential is hardly studied. The biodegradation rates of FeMn alloys have been reported to be lower *in vivo* than *in vitro* [18]. A slower biodegradation rate typically translates into improved biocompatibility of FeMn alloys, due to the decreased amounts of metallic ions released per unit time. Selective laser-melted Fe25Mn alloy (with 66.7% porosity [9]) and Fe35Mn alloy (with 42.6% porosity [10]) have presented *in vitro* biodegradation rates of 0.25 mm/y and 0.42 mm/y, respectively. *In vivo*, another selective laser-melted Fe30Mn alloy (with a porosity range of 37.9 – 47.2%) has shown a volume loss of 10.1 – 20.9% after 48 weeks of implantation [11], corresponding to degradation rates of 0.04 to 0.11 mm/y, which falls outside the desired range of biodegradation rates (*i.e.*, 0.2 – 0.5 mm/y [19]).

A broad spectrum of biofunctionalities is one of the most important prerequisites for biomaterials to be utilized in clinical settings [20]. The concerns regarding the biological response triggered by the porous FeMn alloys may delay their clinical adoption, despite the positive results of a number of *in vivo* studies [10,11]. To address this concern, FeMn alloys have been enriched with Ca [13], Cu [21], Si-Ca [22], and hydroxyapatite [23] to reduce the combined release of Fe and Mn ions and their adverse effects on cells. In addition to Ca, Mg/Si-based bioactive ceramics (*e.g.*, akermanite and bredigite) have shown promise in improving the biological properties of pure Fe [24,25]. The magnesium content of these bioceramics can stimulate the osteogenic differentiation of cells [26], while silicon helps in the synthesis of collagen matrix and bone mineralization [27]. Indeed, adding akermanite (20 vol%) to pure Fe has been shown to enable continuous proliferation of bone cell and the secretion of collagen for biomineralization [25]. However, all these results pertain to pure iron and not FeMn alloys, for which the potential benefits of adding akermanite are unknown.

In this study, we propose 3D printed geometrically ordered porous FeMn-akermanite composites to address all the above-mentioned challenges regarding Fe-based biodegradable metals, including (*i*) low biodegradation rate, (*ii*) MRI incompatibility, (*iii*) uncertain cytotoxicity, and (*iv*) limited bioactivity for bone regeneration. We developed an extrusion-based 3D printing technique *via* an *ex situ* multi-material AM route [28] to fabricate porous FeMn-akermanite composites, which has never been reported in the literature. Based on the fabrication of the composites, we comprehensively evaluated the *in vitro* properties of the composites, including their biodegradation behavior, electrochemical response, magnetic properties, mechanical performance before and after *in vitro* biodegradation. Furthermore, the *in vitro* cytocompatibility of the composites with MC3T3-E1 cells and their osteogenic potential were assessed.

2. Materials and methods

2.1. FeMn-akermanite ink preparation

Fe powder (purity = 99.88 wt%; spherical morphology; particle sizes < 63 µm, Fig. 1**a**) and Mn powder (purity = 99.86 wt%; irregular morphology; particle sizes < 45 µm, Fig. 1**b**) were purchased from Material Technology Innovations Co. Ltd., China. Akermanite powder ($Ca_2MgSi_2O_7$; containing 8.92 wt% Mg; irregular morphology; particle sizes < 45 µm, Fig. 1**c**) was produced from tetraethyl orthosilicate [$(C_2H_5O)_4Si$, TEOS], magnesium nitrate hexahydrate [$Mg(NO_3)_2{\cdot}6H_2O$], and calcium nitrate tetrahydrate [$Ca(NO_3)_2{\cdot}4H_2O$] with a sol-gel method, followed by calcination, as described in [29].

Fe, Mn, and akermanite powder mixtures with 35 wt% Mn and either 20 or 30 vol% akermanite, hereafter referred as Fe35Mn-20Ak and Fe35Mn-30Ak, respectively, were prepared using a roller mixer (CAT Zipperer GmbH, Germany) at 80 rpm for 18 h. The powder mixtures were blended with a hydro-ethanol binder containing 5 wt% hydroxypropyl methylcellulose (hypromellose M_w ~86 kDa, Sigma Aldrich, Germany) [17]. The powder mixture in the inks corresponded to a volume ratio of 47.45%. The rheological characteristics of the inks were determined using an MCR302 rheometer (Anton Paar GmbH, Germany).

2.2. Extrusion-based 3D printing, debinding and sintering

The FeMn-Ak inks were extruded using a 3D BioScaffolder 3.2 printer (GeSiM Bioinstruments and Microfluidics, Germany) in a lay-down pattern design of 0° and 90° switching every other layer

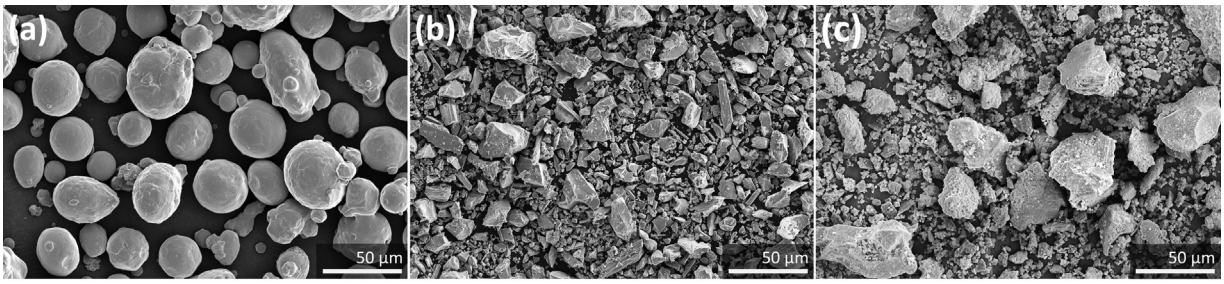

Fig. 1. The morphologies of (a) iron, (b) manganese, and (c) akermanite powders.

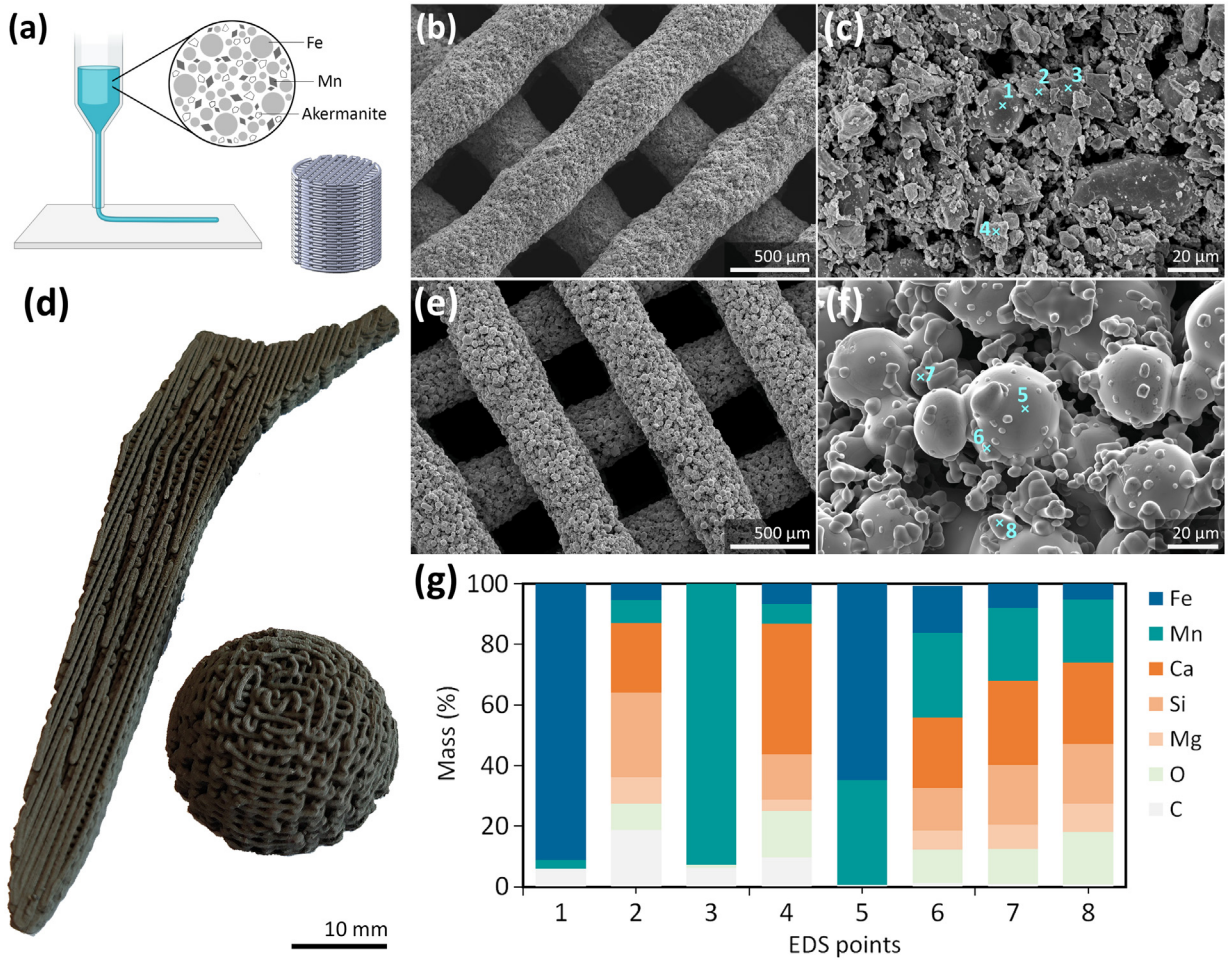

Fig. 2. (a) An illustration of extrusion-based 3D printing and the scaffold design. (b) The morphology of the as-printed Fe35Mn-30Ak specimens and (c) powder particle distribution on the struts. (d) An extrusion-based 3D-printed hip stem as well as a similarly produced acetabular cup. (e) The morphology of the as-sintered Fe35Mn-30Ak specimens and (f) powder particle distribution on the struts. (g) The chemical compositions of the scaffold struts obtained by EDS analysis. The cross signs with a number indicate the locations of the EDS point analyses.

to build cylindrical porous specimens (ϕ = 10 mm, h = 10.5 mm). The porous scaffolds were designed with a strut size of 410 µm, a strut spacing of 400 µm, a layer height of 328 µm, a surface area of 40.4 cm^2, and a relative porosity of 50% (Fig. 2**a**). The extrusion-based 3D printing was performed at a printing speed of 3.5 mm/s under the printing pressures of 325 kPa and 360 kPa for the Fe35Mn-20Ak and Fe35Mn-30Ak inks, respectively. After 3D printing, the green bodies were placed inside a tube furnace (STF16/180, Carbolite Gero Ltd., UK) under highly pure argon flow (purity = 99.9999%). Then, debinding was performed at 350°C for 3 h, followed by sintering at 1200°C for 6 h and then cooling to room temperature. The as-sintered FeMn-Ak scaffolds were ultrasonically cleaned in isopropyl alcohol for 15 min for further investigations.

2.3. Characterization of microstructure, porosity, and phase composition

The shrinkage of the scaffolds in diameter and height due to sintering were measured. The morphology, the struts characteristics (*i.e.*, strut size, strut spacing, layer height, and strut spacing in the *z*-direction), and the chemical composition of the porous FeMn-Ak scaffolds were observed and measured using a scanning electron microscope (SEM, JEOL JSM-IT100, Japan) equipped with energy dispersive X-ray spectroscopy (EDS, JEOL JSM-IT100, Japan). The cross sections of the as-sintered Fe35Mn-30Ak struts were observed using SEM and the elemental compositions were determined using EDS mapping and EDS line analyses (JEOL JSM-IT100, Japan).

In addition, the phases present in the composite scaffolds were identified using an X-ray diffractometer (XRD, D8 Advance, Bruker, USA). The XRD analysis in the Bragg-Brentano geometry was performed using a LynxEye position-sensitive detector with a graphite monochromator under Cu Kα radiation, at 45 kV and 40 mA, with a step size of 0.030° and a counting time of 2 s per step. The XRD results were analyzed using the Diffrac Suite.EVA v6.0 software.

The absolute porosity values of the FeMn-Ak composites were determined, using dry weighing and Eq. (1). The interconnected porosity of the scaffolds was determined by using the oil-impregnation technique and Eq. (2), following the ASTM standard B963-13 [30] based on Archimedes' principle with ethanol as the substitute of water in order to avoid corrosion of the composite specimens:

$$\varphi_a = \left(1 - \frac{m/\rho_{FeMn-Ak}}{V_{bulk}}\right) \times 100\% \quad (1)$$

$$\varphi_i = \left(\frac{\rho_{ethanol}}{\rho_{oil}} \times \frac{m_o - m_a}{m_o - m_{eo}}\right) \times 100\% \quad (2)$$

where φ_a and φ_i are the absolute and interconnected porosities, respectively [%], m is the mass [g] of the as-sintered scaffold, V_{bulk} is the bulk volume [cm^3], $\rho_{FeMn\text{-}Ak}$ is the theoretical density of

the FeMn-Ak composite (*i.e.*, 6.68 g/cm^3 for Fe35Mn-20Ak and 6.22 g/cm^3 for Fe35Mn-30Ak), $\rho_{ethanol}$ is the density of ethanol (*i.e.*, 0.789 g/cm^3), ρ_{oil} is the density of oil (*i.e.*, 0.919 g/cm^3), m_a is the mass of the specimen weighed in air [g], and m_o and m_{eo} are the masses of the oil-impregnated scaffolds weighed in air and in ethanol [g], respectively.

2.4. Measurement of magnetic susceptibility

The magnetic behavior of porous FeMn-Ak specimens (in triplicate, before and after 28 d of *in vitro* biodegradation) was assessed by exposing the specimens to a 2 T magnetic field in a vibrating sample magnetometer (VSM 7307, Lake Shore, USA). Geometrically similar porous pure Fe specimens (*i.e.*, with a lay-down pattern design of 0°/90° angle, strut size = 411 µm, and porosity 67% [31]) were tested as the control group. Magnetic hysteresis loops were obtained and analyzed to determine the saturated and residual magnetization values, as well as the magnetic susceptibility of the specimens.

2.5. In vitro *biodegradation tests*

2.5.1. Static immersion and characterization of the biodegradation products

A revised simulated body fluid (r-SBF) solution [32] with a medium volume of 6.7 mL per 1 cm^2 of the scaffold surface area [33] and an initial pH of 7.40 was used for the *in vitro* biodegradation test of FeMn-Ak composite scaffolds for 1, 4, 7, 14, and 28 d. The surface area of the specimen used for the calculation of the volume of r-SBF was based on the initial scaffold design value. The scaffolds were immersed under static conditions, in a temperature of 37 ± 0.5°C, relative humidity (RH) of 95%, and 5% CO_2 atmosphere. The specimens (in triplicate for each time point) were sterilized before the start of the immersion tests, and the r-SBF medium was filtered using a 0.22 µm pore size filter (Merck Millipore, Germany). During the immersion tests, the pH value of the medium was measured using a pH electrode (InLab Expert Pro-ISM, METTLER TOLEDO, Switzerland).

At the designated time points, the specimens were retrieved to characterize their morphology and determine the chemical composition of biodegradation products using SEM and EDS (JEOL JSM-IT100, Japan). The phases present in the biodegradation products after immersion for 28 d were identified using XRD (D8 Advance, Bruker, USA). The Fe^{2+}, Mn^{2+}, Ca^{2+}, Mg^{2+}, Si^{4+}, and PO_4^{3-} ion concentrations in the medium were measured at various time points using inductively coupled plasma - optical emission spectrometry (ICP-OES, iCAP 6500 Duo, Thermo Scientific, USA).

Furthermore, the biodegradation rates of the FeMn-Ak composites were determined using mass loss measurements. First, the biodegraded scaffolds were immersed in a HCl solution containing hexamethylene tetramine (Sigma Aldrich, Germany) to dissolve the precipitated biodegradation products. The removal cycle is described in detail in our previous publications [17,25,31], following the ASTM standard G1-03 [34]. The remaining scaffold material was weighed and the average biodegradation rate was calculated using Eq. (3), based on the ASTM standard G31-72 [35]:

$$CR_{immersion}\ [mm/year] = 8.76 \times 10^4 \times \frac{m}{A \times t \times \rho} \quad (3)$$

where m is the mass loss value [g], A is the surface area of the porous composite specimen [cm^2] calculated based on the initial scaffold design value, t is the immersion period [h], and ρ is the theoretical density of the FeMn-Ak composite (g/cm^3).

2.5.2. Electrochemical tests

The electrochemical characteristics of the porous FeMn-Ak composites were studied using a Bio-Logic SP-200 potentiostat (Bio-Logic Science Instruments, France) with the setup and parameters described in our previous publications [17,25,31]. Briefly, the potentiostat consisted of three electrodes, including an Ag/AgCl electrode as the reference electrode, a graphite bar as the counter electrode, and the porous specimen partially embedded in an acrylic resin as the working electrode. Potentials reported are *vs.* Ag/AgCl reference electrode unless stated differently. The corrosion medium was r-SBF [32] with an initial pH of 7.40. The temperature was maintained at 37 ± 0.5°C. The exposed surface area of the specimens was calculated, based on their initial designs. Linear polarization resistance (LPR) and electrochemical impedance spectroscopy (EIS) measurements were performed for up to 28 d. The LPR values were measured at a scanning rate of 0.167 mV/s from -25 to +25 mV *vs.* OCP. The EIS tests were performed at frequencies ranging between 100 kHz and 10 mHz using a 10 mV sine amplitude *vs.* OCP.

2.6. Mechanical characterization

The compressive mechanical properties of the porous FeMn-Ak composites were evaluated before and after *in vitro* biodegradation tests (in triplicate) using a universal mechanical testing machine with a 100 kN load cell (Zwick Z100, Germany). The compression tests were conducted, following the ISO standard 13314:2011 [36], at a crosshead speed of 3 mm/s. The strain values were determined, based on the deformation of the specimen. From the stress-strain curves, the compressive 0.2% offset stress (referred to as the yield strength) and the quasi elastic gradient (referred to as the Young's modulus) were determined. The yield strength value was the stress value at the intersection of the stress-strain curve with a line (0.2% offset) parallel to the linear region of the stress-strain curve. The Young's modulus value was determined as the slope of the linear region of the stress-strain curve. The initial toe region of the stress-strain curves was not considered in the calculation of the yield strength and Young's modulus.

2.7. Cytocompatibility evaluation

2.7.1. Preculture of preosteoblasts and preparation of FeMn-Ak composites extracts

Murine preosteoblasts (MC3T3-E1, Sigma Aldrich, Germany) were cultured in a flask in a cell culture incubator (temperature = 37 ± 0.5°C, relative humidity (RH) = 95%, CO_2 content = 5%). The cell culture medium contained the α-minimum essential medium (α-MEM) supplemented with 10% fetal bovine serum (FBS) and 1% penicillin/streptomycin (p/s). The cell culture medium components were purchased from Thermo Fisher Scientific, USA.

The extracts of the composite specimens were obtained by incubating the sterile specimens (ϕ = 10.2 mm, h = 10.6 mm) in the cell culture medium (with a ratio of 1 mL per 5 cm^2 specimen surface area) for 72 h [37]. The surface area of the composites was calculated, using their initial design. Thereafter, the extracts were retrieved and filtered through a 0.22 µm pore (Merck Millipore, Germany). The concentrations of Fe^{2+}, Mn^{2+}, Ca^{2+}, Mg^{2+}, and Si^{4+} ions in the extracts were measured using ICP-OES (iCAP 6500 Duo, Thermo Scientific, USA).

2.7.2. Indirect cell culture and metabolic activity assay

Murine preosteoblasts (MC3T3-E1, 1 × 10^4 cells per well) were cultured in triplicate in a 48-well plate containing 200 µL of the above-described extracts. Preosteoblasts cultured in the normal cell culture medium were used as the negative control. After 1, 3, and 7 d of cell culture, the metabolic activity of cells was evaluated using PrestoBlue assay, following procedure described in our previous

publications [17,25,31]. The PrestoBlue reagent (Thermo Fisher Scientific, USA) was added to the wells, followed by incubation for 1 h and the measurement of the absorbance values using a microplate reader at a wavelength of 570 nm (Victor X3, PerkinElmer, USA). The metabolic activity of the cells was determined as:

$$\text{Metabolic activity [\%]} = \frac{\text{Absorbance (specimen)}}{\text{Absorbance (negative control)}} \times 100 \quad (4)$$

2.7.3. Direct culture of cells on the specimens with live-dead staining and SEM imaging

Murine preosteoblasts (MC3T3-E1, 5×10^4 cells per specimen) were cultured on the FeMn-Ak specimens (ϕ = 7.0 mm and h = 0.6 mm) in 6-well plates containing 8 mL of cell culture medium. Osteogenic cell culture medium (made of α-MEM, supplemented with 10% FBS, 1% p/s, 1:1000 ascorbic acid, and 1:500 β-glycerophosphate) was used from day 2 onwards. The specimens were cultured for 7 and 21 d (in triplicate for each of the time points). The viability of cells on the composite specimens was determined using calcein and ethidium homodimer-1 staining (Thermo Fisher Scientific, USA), following the procedure described in our previous publications [17,25,31]. The morphology of the cells was observed using SEM (JEOL JSM-IT100, Japan). Geometrically similar porous Ti6Al4V (*i.e.*, with a lay-down pattern design of 0°/90° angle, made by means of selective laser melting) and Fe-35Mn alloy (*i.e.*, with a lay-down pattern design of 0°/90° angle, strut size = 412 µm, and porosity 69% [17]) specimens were used as the controls for the cell morphology evaluation at the selected time points.

2.7.4. Immunostaining of osteogenic markers

The immunostaining of the MC3T3-E1 cells cultured on the composite specimens was performed at day 14 for Runt-related transcription factor 2 (Runx2) and at day 21 for osteopontin (OPN). A similar procedure as described in our previous publication [25] was followed. Briefly, at the designated time points, the specimens were washed with phosphate buffer saline (PBS) and were fixed using 4% paraformaldehyde for 15 min, followed by permeabilization using 0.5% Triton/PBS for 5 min at 4°C (Sigma Aldrich, Germany). Consecutively, the specimens were individually incubated in well-plates containing 1% bovine serum albumin (BSA)/PBS for 5 min at 37°C. In this study, the primary antibodies of anti-Runx2 anti-rabbit (1:250 per specimen, Abcam, UK) and anti-OPN anti-mouse (1:100 per specimen, Santa Cruz Biotechnology, USA) were added, and the specimens were incubated at 37°C for 1 h. Thereafter, the specimens were washed 3 times using 0.5% Tween/PBS (Sigma Aldrich, Germany), followed by an incubation step at 37°C for 1 h in 1% BSA/PBS containing conjugated secondary antibodies of Alexa Fluor 488 anti-rabbit (1:200, Thermo Fischer Scientific, USA) and Alexa Fluor 594 anti-mouse (1:100, Thermo Fischer Scientific, USA). Subsequently, the specimens were washed 3 times using 0.5% Tween/PBS prior to imaging using a microscope (ZOE cell imager, Bio-Rad, USA). Geometrically similar porous Ti6Al4V specimens (*i.e.*, with a lay-down pattern design of 0°/90° angle, made by selective laser melting) were used as the controls for the Runx2 staining at day 14.

2.8. Statistical analysis

The statistical analysis of the PrestoBlue results was performed using a two-way ANOVA, followed by a Tukey multiple comparison *post hoc* test (**** = $p < 0.0001$, *** = $p < 0.001$, ** = $p < 0.01$, and * = $p < 0.05$, *n.s.* = not significant).

3. Results

3.1. Characteristics of the porous FeMn-Ak composite scaffolds

Extrusion-based 3D printing was successful in fabricating porous FeMn-Ak scaffolds (Fig. 2**a**). The design of the lay-down pattern was such that the struts bridged above the underlying layers at 0° and 90° angles (Figs. 2**b, S2, S3**). The FeMn-20Ak had a diameter (ϕ) of 10.04 ± 0.01 mm and a height (h) of 10.46 ± 0.02 mm. The FeMn-30Ak had a diameter (ϕ) of 10.02 ± 0.03 mm and a height (h) = 10.47 ± 0.04 mm. All these values are very close to the initial design values (ϕ = 10 mm; h = 10.5 mm). In addition to the cylindrical specimens, the extrusion-based 3D printing was capable of fabricating geometrically complex implants (*e.g.*, hip stem and acetabular components (Fig. 2**d**)). Given that the success in 3D printing strongly depends on adequate powder loading in the ink as well as its rheological behavior, viscosity and shear stress of the FeMn-akermanite-containing inks as a function of shear rate were determined to confirm the shear-thinning behavior (**Fig. S1**). On the struts of the green-body scaffolds (Fig. 2**b**), individual powder particles (*i.e.*, Fe, Mn, and akermanite) could still be discerned (Fig. 2**c**), together with a relatively high mass% of carbon from the hypromellose binder (*i.e.*, 6–19%, Fig. 2**g**, EDS points 1-4).

After debinding and sintering, the FeMn-Ak composite scaffolds maintained the original geometrical design (Figs. 2**e, S2**) with minimal expansions of 1–1.5% in height and 1.4–1.8% in diameter. The measured mean values of the strut size, strut spacing, layer height, and strut spacing in z-direction are listed in Table 1. The struts of the specimens featured an open micro-porous architecture with absolute porosities of 69% and 70% (± 3%) for Fe35Mn-20Ak and Fe35Mn-30Ak, respectively. The interconnected porosity of both types of the composite scaffolds was 69% ± 1%. The spherical particles found on the periphery of the Fe35Mn-30Ak struts were composed of Fe and Mn (EDS point 5 in Fig. 2**f-g**). These spherical powder particles were decorated and occasionally connected by irregularly shaped particles that were mainly composed of Ca, Mg, Si, and O, in addition to traces of Fe and Mn (Fig. 2**f-g**, EDS points 6 to 8). Similar observations were made for the Fe35Mn-20Ak specimens (**Fig. S2**). After sintering, the mass percentages of carbon on the struts of both types of the scaffolds (*i.e.*, 0.6–1.2%, Fig. 2**g**, EDS points 5 to 8) were significantly decreased as compared to those of the green bodies.

On the cross sections of the Fe35Mn-30Ak specimens, EDS mapping analysis indicated the diffusion of Fe and Mn into the akermanite particles (highlighted by boxes in Fig. 3**a**). The depths of the elemental diffusion of Fe and Mn into the akermanite phase were measured to be ≈ 4.9 µm and > 28 µm, respectively (Fig. 3**b**). XRD analysis revealed the presence of the γ-FeMn phase in the specimens, thereby confirming the successful *in situ* alloying of Fe with Mn during sintering (Fig. 4**a**). In addition, the nesosili-

Table 1
The geometric characteristics of the extrusion-based 3D printed FeMn-Ak composite scaffolds.

Sample group	Strut width (µm)	Strut spacing (µm)	Layer height (µm)	Strut spacing in *the z* direction (µm)
Fe35Mn-20Ak	419 ± 3	391 ± 3	325 ± 5	235 ± 6
Fe35Mn-30Ak	414 ± 3	395 ± 4	326 ± 8	240 ± 8

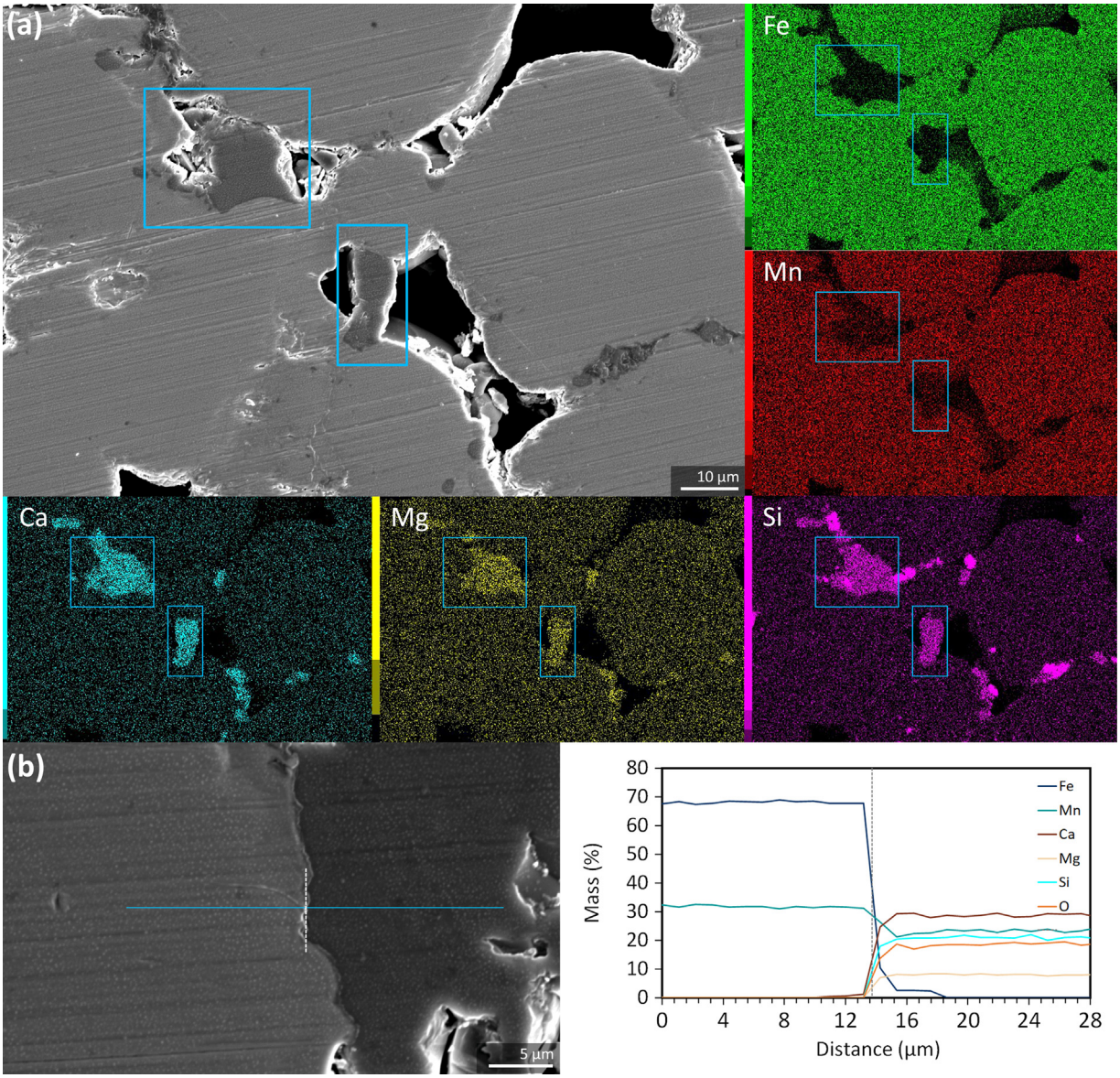

Fig. 3. The cross sections of the composite struts: (a) EDS mapping analysis in the region of interest, and (b) EDS line analysis across the interface of the FeMn alloy and the bioceramic.

cate crystalline phases, including kirschsteinite ($Ca(Fe)SiO_4$), glaucochroite ($Ca(Mn)SiO_4$), and monticellite ($Ca(Mg)SiO_4$), were identified (Fig. 4**a**). The intensities of the nesosilicate phases were higher in the specimens containing with more akermanite.

3.2. Magnetic properties

The saturated magnetization of the FeMn-Ak composites in the presence of 2 T magnetic field (*i.e.*, 0.64 Am^2/kg for Fe35Mn-20Ak and 0.71 Am^2/kg for Fe35Mn-30Ak, Fig. 4**c**) was 2–3 orders of magnitude lower than that of comparable pure Fe scaffolds (*i.e.*, 190 Am^2/kg). The residual magnetism values of the porous composites were low too (*i.e.*, 0.05 and 0.06 Am^2/kg for Fe35Mn-20Ak and Fe35Mn-30Ak, respectively). After 28 d of biodegradation (Fig. 4**d**), the saturation magnetization values of the porous FeMn-Ak scaffolds only slightly increased (to 0.9 Am^2/kg) but nevertheless remained multiple orders of magnitude below that of pure Fe. Along with *in vitro* biodegradation, the residual magnetism values of the porous composites decreased to 0.03 and 0.02 Am^2/kg, respectively. The magnetic susceptibility values of the porous composites were 3.6 ± 0.2 ($\times 10^{-3}$) for Fe35Mn-20Ak and 3.7 ± 0.4 ($\times 10^{-3}$) for Fe35Mn-30Ak. After 28 d of biodegradation, the values remained low (*i.e.*, 4.0 ± 0.4 ($\times 10^{-3}$) and 4.5 ± 0.9 ($\times 10^{-3}$) for Fe35Mn-20Ak and Fe35Mn-30Ak, respectively). As for the ferromagnetic pure Fe, the magnetic susceptibility value was 5.08 ± 0.05, which was three orders of magnitude higher than the values of the porous FeMn-Ak composites scaffolds.

3.3. Biodegradability and the characteristics of the biodegradation products

During the *in vitro* biodegradation tests, the typical yellow-brownish layer of Fe-based biodegradation products formed on the specimens (Fig. 5**a**). Initially (*i.e.*, at day 4), the scaffolds exhibited a high biodegradability, with corrosion rates of 1.27 ± 0.01 mm/y for Fe35Mn-20Ak and 1.36 ± 0.06 mm/y for Fe35Mn-30Ak. However by day 28, the *in vitro* biodegradation rates of the porous composites reduced to 0.24 ± 0.01 mm/y and 0.27 ± 0.04 mm/y, for Fe35Mn-20Ak and Fe35Mn-30Ak, respectively (Fig. 5**b**). Until the

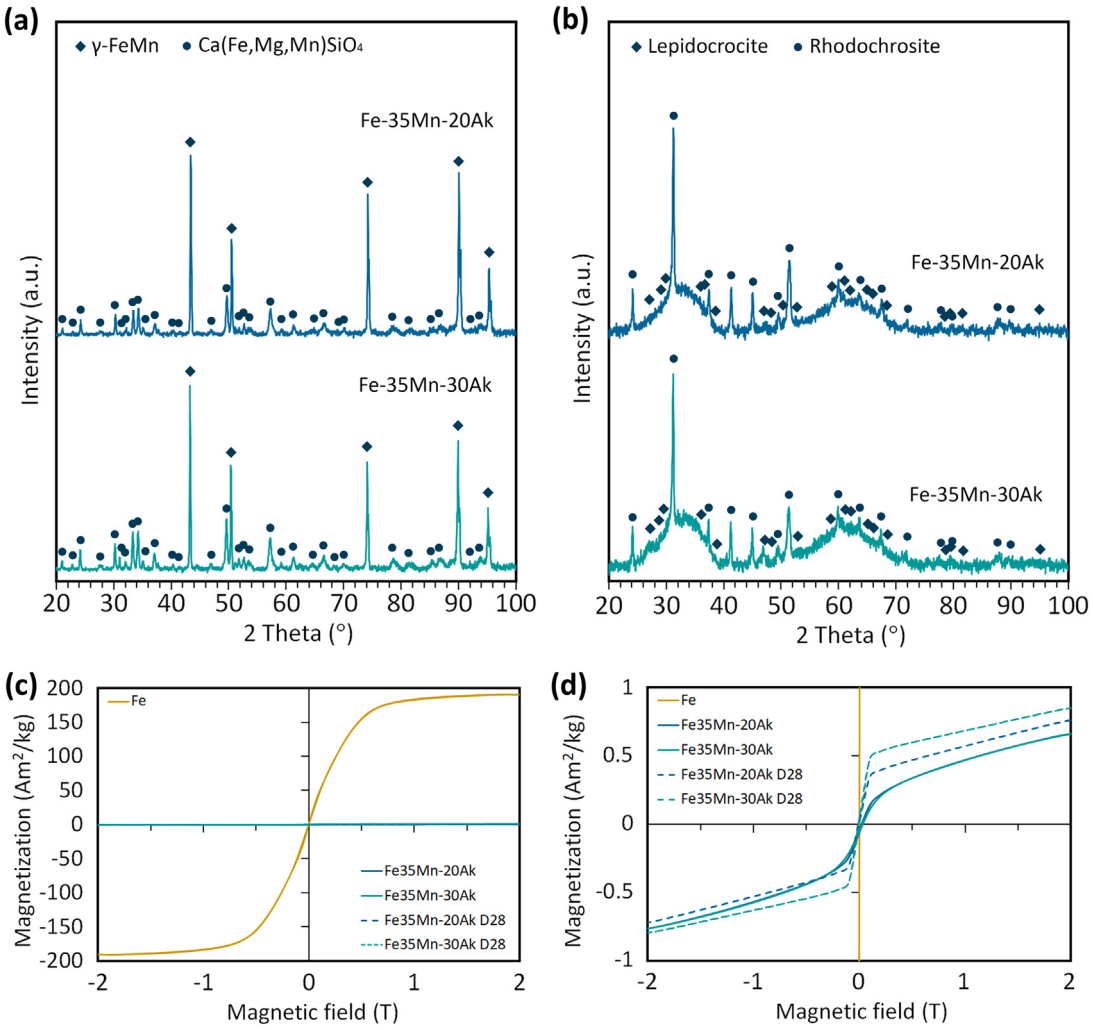

Fig. 4. The phase compositions of the composite scaffolds: (a) as-sintered and (b) after *in vitro* biodegradation for 28 d. (c, d) The magnetization curves of the FeMn-Ak specimens (as-sintered and after *in vitro* biodegradation for 28 (d) at different graph scales in comparison with pure Fe.

end of the immersion tests (28 d), the global pH values of the r-SBF medium remained between 7.64 and 7.68, due to the controlled 5% CO_2 atmosphere in the incubator.

SEM (Fig. 5**c-e**) revealed that the struts of the composite scaffolds were encapsulated by the degradation products that accumulated over the immersion time. The morphologies of the biodegradation products on the periphery could be discerned from a particulate structure to a denser phase over time. The biodegradation products were composed of a mixture of Fe, Mn, C, and O elements (Fig. 5**f-h, S4**). In addition, the biodegradation products on the struts of Fe35Mn-30Ak specimens contained Ca and P at all time points (Fig. 5**f-h**). In the degradation products of the Fe35Mn-20Ak scaffolds, however, only Ca was detected (**Fig. S4**). The phases present in the biodegradation products of the porous specimens after 28 d of immersion were lepidocrocite (γ-FeOOH) and rhodochrosite ($MnCO_3$, Fig. 4**b**), which corresponded to the main chemical compositions identified by EDS. At the center of the composite scaffolds (Fig. 5**i, S4**), the biodegradation products had formed over the pore networks of the struts and were largely composed of oxides. After biodegradation, the initially spherical Fe-Mn particles were decorated by irregularly shaped nesosilicate particles (Fig. 2**f**) and exhibited rough particle surface characteristics, indicating localized corrosion that occurred on the interfaces of the powder particles (indicated by arrows in Fig. 5**i**). Overall, the nesosilicate particles (mainly composed of Ca, Mg, Si, and O) could still be identified at the center of the composites (Fig. 5**i, S4**).

The concentrations of Fe^{2+}, Mn^{2+}, Ca^{2+}, PO_4^{3-}, Mg^{2+}, and Si^{4+} ions in the r-SBF medium were measured during the course of the immersion tests (Fig. 6). Fe^{2+} ions were steadily released from both the Fe35Mn-20Ak and Fe35Mn-30Ak specimens over time (*i.e.*, from 0.23 ± 0.02 mg/L and 0.34 ± 0.02 mg/L at day 4 to 0.90 ± 0.02 mg/L and 0.93 ± 0.06 mg/L at day 28, respectively, Fig. 6**a**). The concentration of the Mn^{2+} ions released from the Fe35Mn-30Ak specimens was the highest at day 7 (*i.e.*, 11.0 ± 0.3 mg/L), followed by a decreasing trend towards the end of the immersion tests at day 28 (*i.e.*, 9.4 ± 0.4 mg/L). Mn^{2+} ions were continuously released from the Fe35Mn-20Ak specimens and the concentration increased from 6.2 ± 0.1 mg/L at day 4 up to 11.4 ± 0.3 mg/L at day 28 (Fig. 6**b**). The Ca^{2+} ion concentrations in the r-SBF medium decreased throughout the immersion period for all the composite specimens similarly (*i.e.*, from 76 ± 1 mg/L and 79 ± 4 mg/L at day 4 to 28 ± 1 mg/L at day 28, Fig. 6**c**). In a similar trend, the PO_4^{3-} ion concentration decreased over time, with a larger reduction observed for the Fe35Mn-30Ak specimens during the first 7 days of immersion (Fig. 6**d**). Moreover, the Mg^{2+} ion concentration in the r-SBF medium marginally increased over time, with the highest Mg^{2+} ion concentrations registered at day 4 (*i.e.*, 46.7 ± 0.3 mg/L for Fe35Mn-20Ak and 48 ± 2 mg/L for Fe35Mn-30Ak, Fig. 6**e**). The concentration of Si^{4+} ion increased

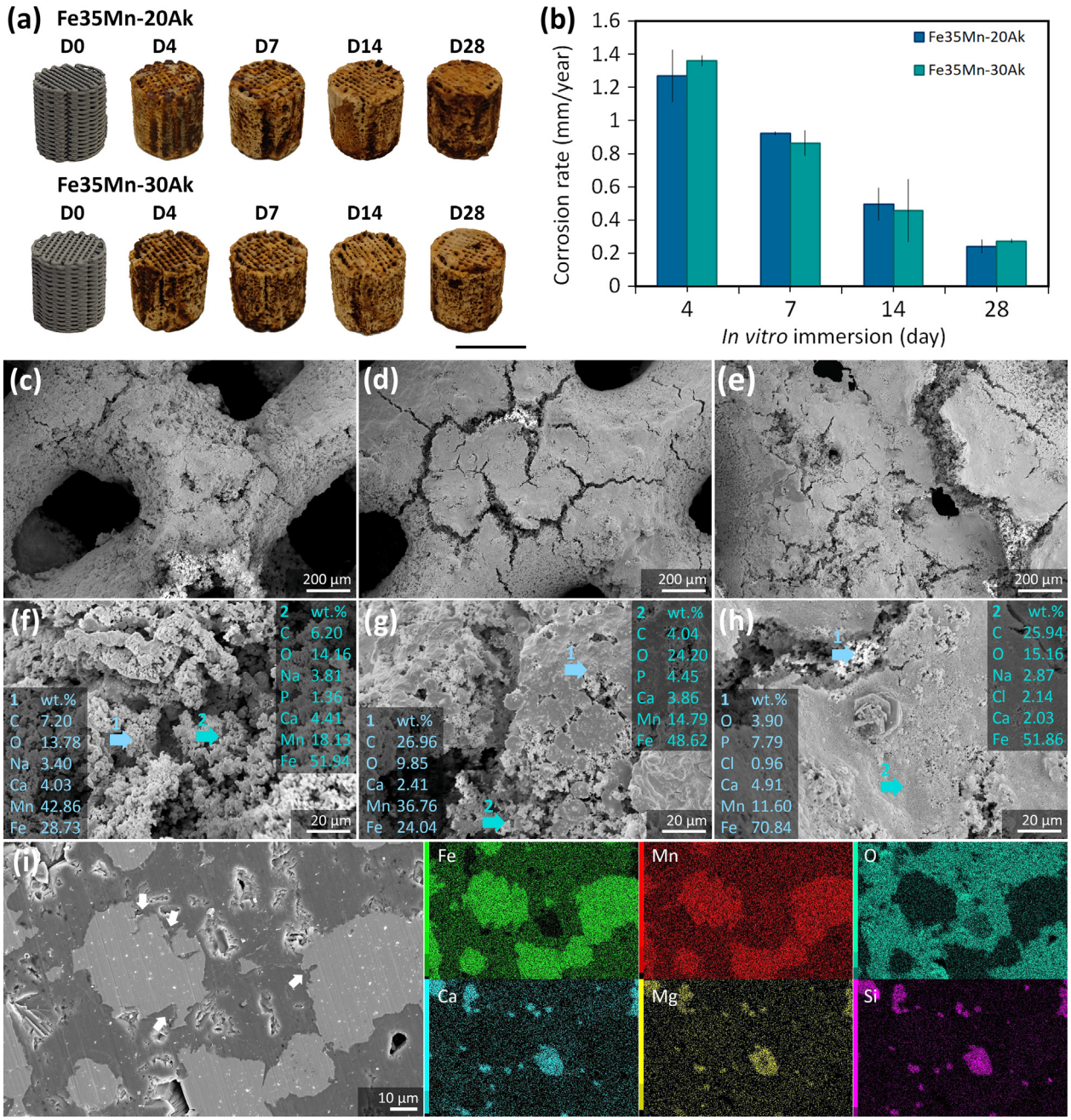

Fig. 5. The *in vitro* biodegradation characteristics of the porous composite scaffolds: (a) The visual inspection of the scaffolds before and after *in vitro* biodegradation at different time points (scale bar = 10 mm) and (b) the corresponding corrosion rates. (c-e) The morphologies and (f-h) chemical compositions of the biodegradation products on the periphery of the Fe35Mn-30Ak specimens after (c, f) 4, (d, g) 7, and (e, h) 28 d of biodegradation as well as (i) at the central location inside the specimens after 28 d of biodegradation. The arrow indicates the locations of the EDS point analyses.

from 2.83 ± 0.3 mg/L and 3.8 ± 0.2 mg/L at day 4 to 3.9 ± 0.1 mg/L and 3.9 ± 0.3 mg/L at day 28 for the Fe35Mn-20Ak and Fe35Mn-30Ak specimens, respectively (Fig. 6**f**).

3.4. Electrochemical measurements

Both the porous FeMn-Ak composites demonstrated decreasing OCP values during the 28 d of biodegradation (Fig. 7**a**). At day 1, the OCP values were -646 ± 9 mV for Fe35Mn-20Ak and -643 ± 23 mV for Fe35Mn-30Ak. At day 28, the OCP values decreased to -692 ± 7 mV and -673 ± 3 mV for the Fe35Mn-20Ak and Fe35Mn-30Ak specimens, respectively. The polarization resistance (R_p) values of the porous composites were 5 ± 2 kΩ.cm^2 for Fe35Mn-20Ak and 8 ± 2 kΩ.cm^2 for Fe35Mn-30Ak at day 4 of immersion, which then increased to 10 ± 2 kΩ.cm^2 and 11 ± 2 kΩ.cm^2 at day 14 of immersion, respectively (Fig. 7**b**). At day 28, R_p stabilized at the values of 9.3 ± 0.4 kΩ.cm^2 and 10.5 ± 0.4 kΩ.cm^2, respectively, for the Fe35Mn-20Ak and Fe35Mn-30Ak specimens. The Bode impedance modulus values of the porous composites at a low frequency of 0.01 Hz stabilized or only slightly increased over the immersion period (Fig. 7**c-d**). At day 4, the impedance modulus magnitudes were 3.7 ± 0.3 kΩ.cm^2 and 3.8 ± 0.9 kΩ.cm^2 for the Fe35Mn-20Ak and Fe35Mn-30Ak specimens, respectively. At day 28, the impedance modulus magnitudes had stabilize or marginally increased to 3.9 ± 0.1 kΩ.cm^2 for both types of composites. At the mid-frequency of 100 Hz,

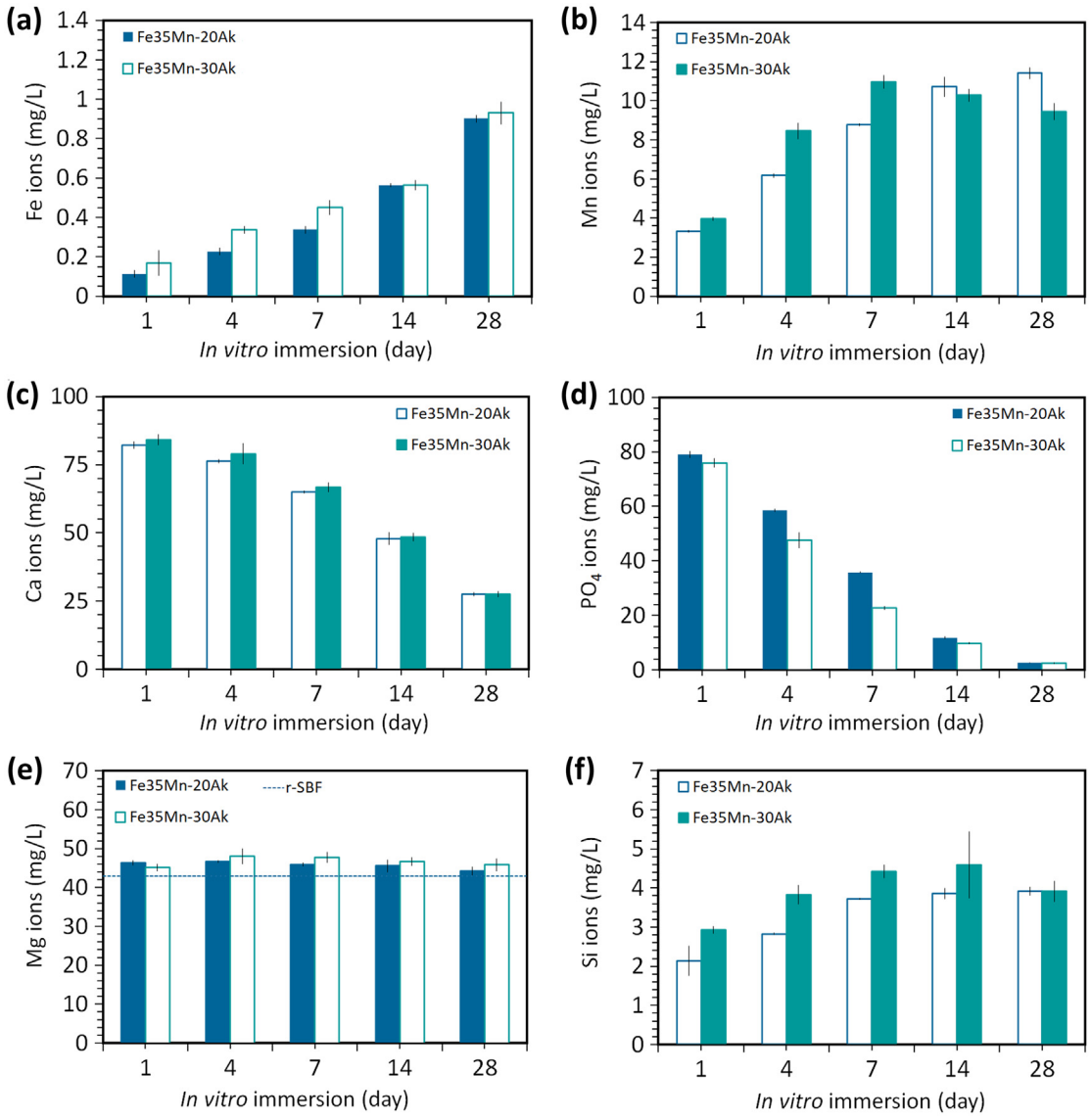

Fig. 6. The concentrations of (a) Fe, (b) Mn, (c) Ca, (d) PO_4, (e) Mg, and (d) Si ions in the r-SBF medium over biodegradation time. The dotted line indicates the initial concentration of Mg ions in the medium.

the Bode impedance modulus values of the Fe35Mn-20Ak specimens were relatively stable (*i.e.*, 2.5 ± 0.1 kΩ.cm^2 at day 4 and 2.5 ± 0.2 kΩ.cm^2 at day 28 of immersion, Fig. 7**c**). The Bode impedance modulus values of the Fe35Mn-30Ak specimens at the mid-frequency of 100 Hz slightly decreased over time from 2.82 ± 0.05 kΩ.cm^2 at day 4 to 2.57 ± 0.03 kΩ.cm^2 at day 28 of immersion (Fig. 7**d**). Furthermore, the peak of the Bode plot phase angle did not shift during the biodegradation tests of the Fe35Mn-20Ak and Fe35Mn-30Ak specimens, and remained in the high frequency region (*e.g.*, 1–10 kHz) (Fig. 7**c-d**). The Bode plot phase angles at high frequencies (*e.g.*, 10 kHz) were relatively stable between -8° to -12° for the Fe35Mn-20Ak and Fe35Mn-30Ak specimens over the entire period of the immersion tests.

3.5. Mechanical properties

The composite scaffolds exhibited stress-strain curves with initial linear elastic deformation, followed by plastic deformation, resembling the typical strain-hardening behavior of porous materials (Fig. 8**a-b**). The composite scaffolds (*i.e.*, Fe35Mn-20Ak and Fe35Mn-30Ak) had yield strengths of 8.3 ± 0.6 MPa and 3.1 ± 0.4 MPa, respectively. The Young's modulus values were 0.53 ± 0.03 GPa and 0.25 ± 0.04 GPa, respectively. Due to biodegradation, the yield strength of the Fe35Mn-20Ak specimens reduced to 4.1 ± 0.7 MPa at day 7, and to 1.8 ± 0.6 MPa at day 28 (Fig. 8**c**). The Young's modulus of the Fe35Mn-20Ak specimens also decreased to 0.17 ± 0.02 GPa, respectively, at day 7, and to 0.09 ± 0.01 GPa at day 28 (Fig. 8**d**). For the Fe35Mn-30Ak specimens, the yield strength and Young's modulus decreased to 2.5 ± 0.7 MPa and 0.17 ± 0.06 GPa after 7 days. The Fe35Mn-30Ak scaffolds did not exhibit strain-hardening after 14 and 28 d of biodegradation (Fig. 8**b**). The compressive strength values were 4.5 ± 0.3 MPa at day 14, which decreased to 3.9 ± 0.9 MPa at day 28 (Fig. 8**c**), while the Young's modulus values were reduced to 0.057 ± 0.005 GPa at day 14 and 0.034 ± 0.009 GPa at day 28 (Fig. 8**d**).

3.6. Metabolic activity of cells cultured with the extracts of the composites

The Fe35Mn-20Ak extracts contained 61 ± 2 mg/L of Fe^{2+} ions, 35.3 ± 0.6 mg/L of Mn^{2+} ions, 73.3 ± 0.6 mg/L of Ca^{2+}

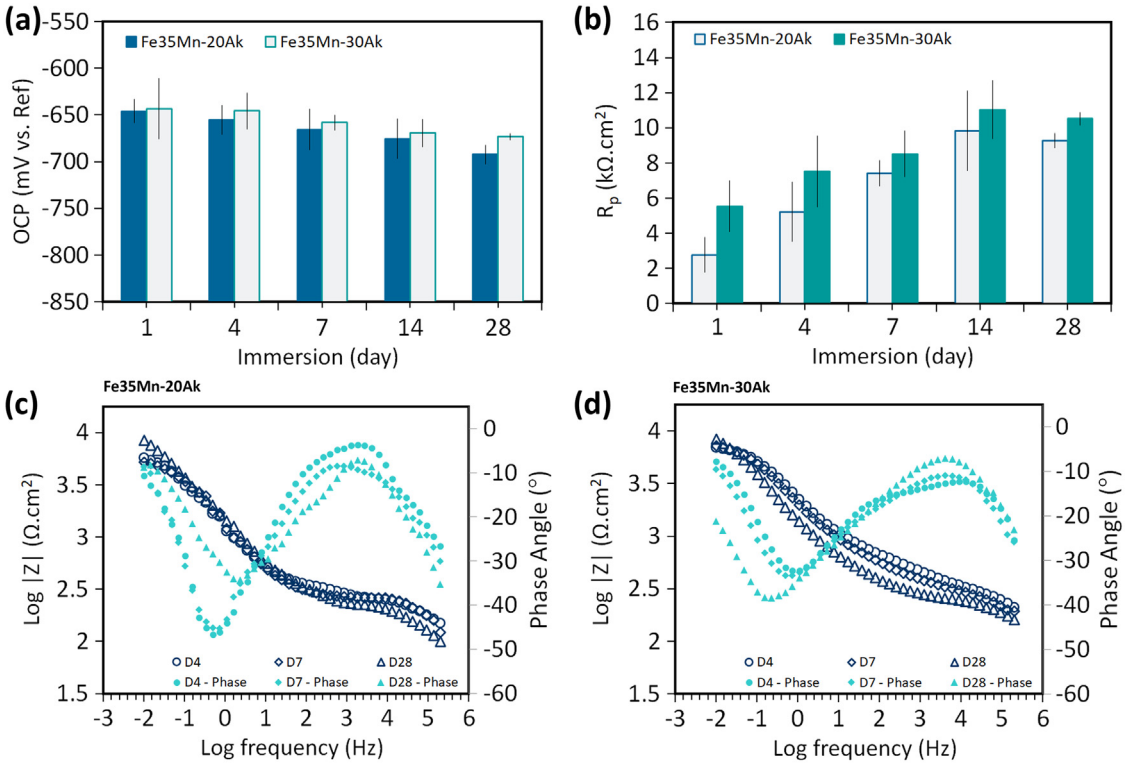

Fig. 7. The electrochemical response of the porous composite scaffolds during 28 d of biodegradation: (a) OCP and (b) R_p values from the LPR tests. The impedance modulus and phase angle Bode plots at the selected time points for the (c) Fe35Mn-20Ak and (d) Fe35Mn-30Ak scaffolds.

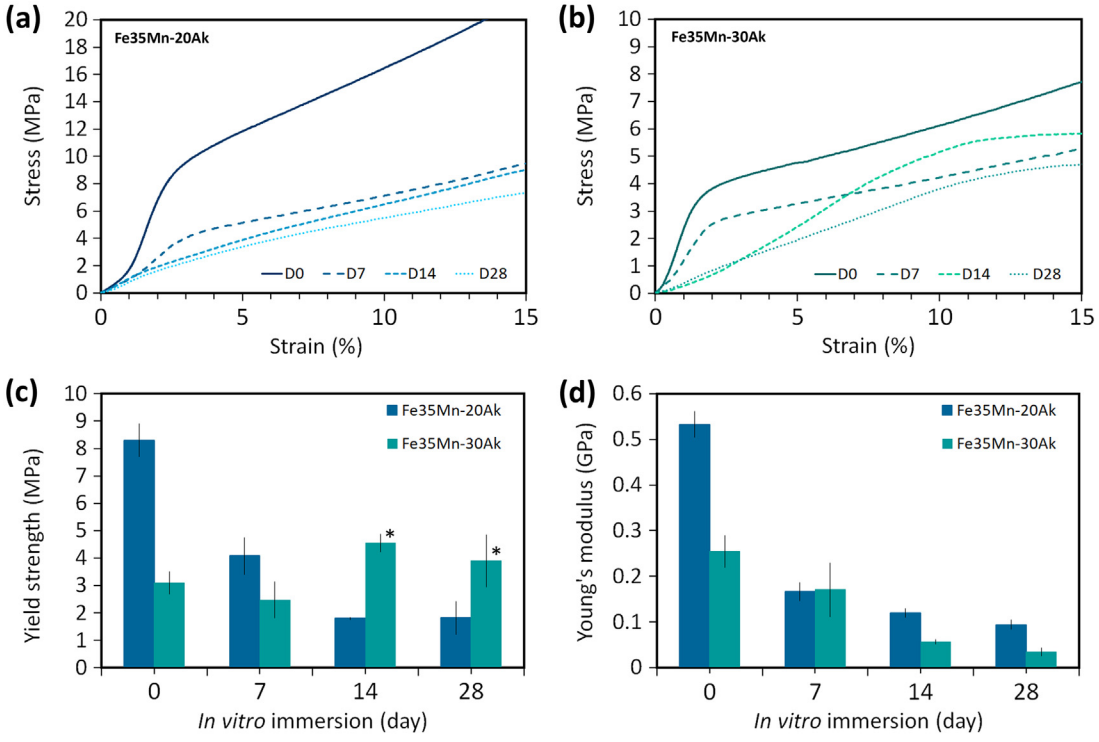

Fig. 8. The compressive mechanical properties of the porous composite scaffolds: the stress-strain curves of the (a) Fe35Mn-20Ak and (b) Fe35Mn-30Ak scaffolds, and variations of (c) yield strength and (d) Young's modulus with biodegradation time. The asterisk symbols indicate the compressive strength values of the Fe35Mn-30Ak scaffolds after 14 and 28 d of biodegradation.

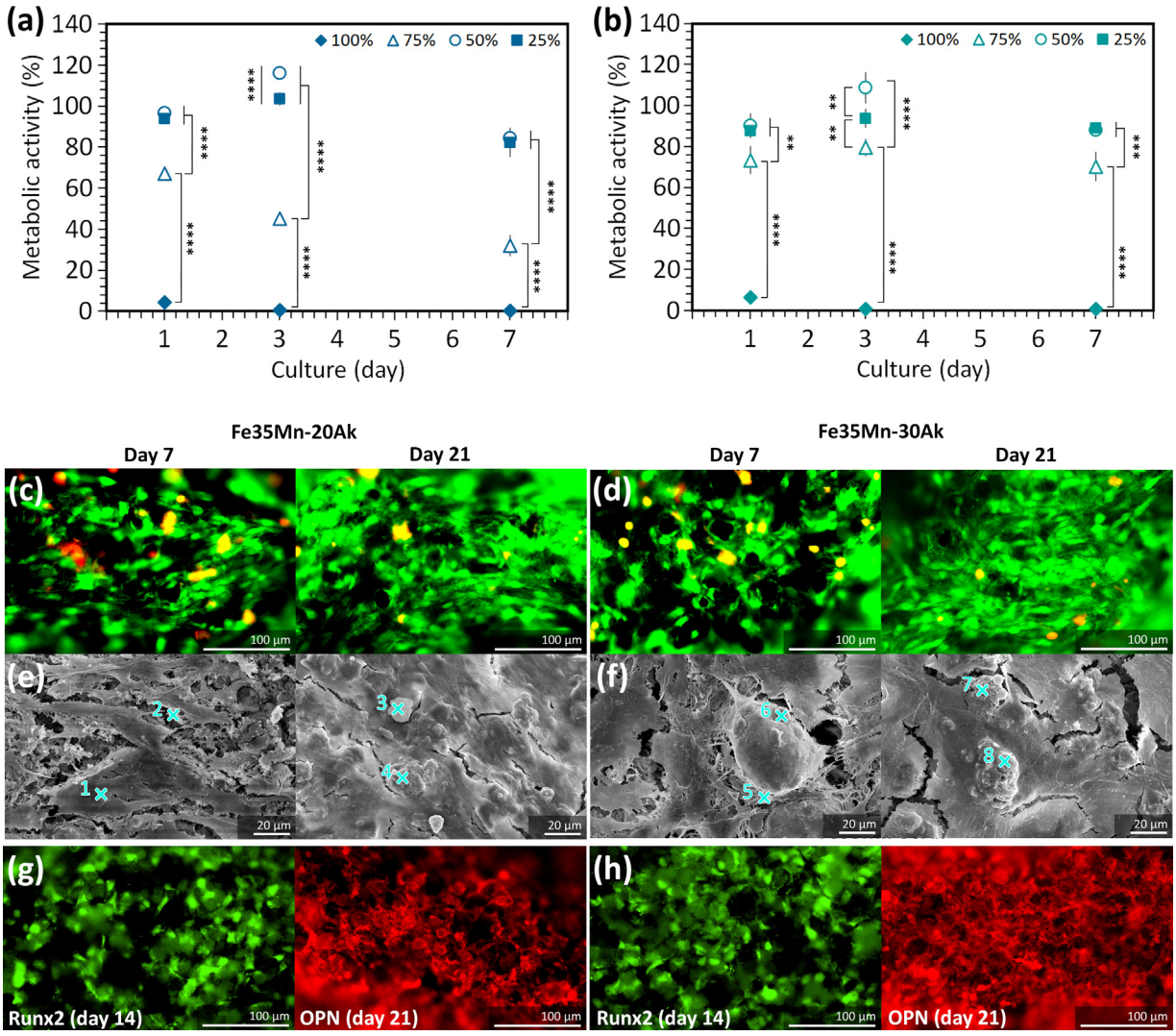

Fig. 9. The cytocompatibility and bioactivity of the porous composite scaffolds assessed using the MC3T3-E1 preosteoblasts: the metabolic activity of the cells after culture with the extracts of the (a) Fe35Mn-20Ak and (b) Fe35Mn-30Ak specimens. The live/dead staining and morphology of the cells cultured on the (c, d) Fe35Mn-20Ak and (e, f) Fe35Mn-30Ak specimens at day 7 and 21. (g-h) The immunostaining of Runx2 at day 14 and OPN at day 21. **** = $p < 0.0001$, *** = $p < 0.001$, and ** = $p < 0.01$.

ions, 40.7 ± 0.6 mg/L of Mg^{2+} ions, and 6 ± 1 mg/L of Si^{4+} ions. In the Fe35Mn-30Ak extracts, the ionic concentrations were 68.7 ± 1.2 mg/L of Fe^{2+}, 30.3 ± 0.6 mg/L of Mn^{2+}, 104 ± 2 mg/L of Ca^{2+}, 36.3 ± 0.6 mg/L of Mg^{2+}, and 7.3 ± 0.1 mg/L Si^{4+}. The preosteoblasts were metabolically active (grade 1, non-toxic [38]) in the composite extracts of 25% and 50% (Fig. 9**a-b**). In the 75% extracts of Fe35Mn-20Ak (Fig. 9**a**), the preosteoblasts showed a decline in their metabolic activity (grade 2, fairly reactive [38]). However, in the 75% extracts of Fe35Mn-30Ak, the cells were still metabolically active (Fig. 9**b**, grade 1, non-toxic [38]). The cellular metabolic activities were suppressed (grade 4, severely reactive [38]) only when cultured with the 100% extracts.

3.7. Morphology and osteogenic differentiation of cells on the composites

Live/dead fluorescent images showed the viability of the preosteoblasts cultured on the composite specimens after 7 and 21 d (Fig. 9**c-d**). The preosteoblasts adhered on the surfaces of the composites and exhibited a spread morphology with extended filopodia (**Fig. S5**). A monolayer of cells formed after 7 d, covering the struts of the specimens (Fig. 9**e-f**). The cell layer thickened at day 21 (Fig. 9**e-f**), showing that cells proliferated over time and produced extracellular matrix on the composite specimens, which was comparable to those observed on Ti6Al4V specimens (**Fig. S6**). Moreover, the preosteoblasts cultured on the FeMn-Ak composite specimens exhibited cues of osteogenic differentiation. The Runx2 was expressed at day 14, showing that the osteogenic differentiation of the cells had occurred (Fig. 9**g-h**), comparable to the levels observed for the Ti6Al4V specimens (**Fig. S6**). The cells were surrounded by precipitates, which were more clearly visible on day 21. The precipitates were integrated into the cell layers and contained Ca and P (Table 2). This observation was further supported by the presence of OPN at day 21 (Fig. 9**g-h**). A higher intensity of OPN could be observed on the Fe35Mn-30Ak specimens relative to the Fe35Mn-20Ak specimens.

4. Discussion

The developed porous biomaterials made of Fe, Mn, and akermanite show a significantly improved performance for biodegradable bone implant applications. The FeMn-Ak composite scaffolds produced by extrusion-based 3D printing demonstrated (i) enhanced biodegradability at the rates of 0.24–0.27 mm/y that are in the suggested range of suitable biodegradation rates for ideal bone substitutes (*i.e.*, 0.2–0.5 mm/y [19]); (ii) a very low saturated

Table 2
The chemical compositions of the biodegradation products on the composites during cell culture as determined by EDS analysis.

EDS points		C	O	Na	P	K	Ca	Mn	Fe
Fe35Mn-20Ak	**1**	19 ± 2	18 ± 7	6 ± 2	14 ± 3	-	10 ± 1	7 ± 1	25 ± 3
D7	**2**	16 ± 1	28 ± 5	9 ± 5	9 ± 4	1.8 ± 0.3	9 ± 3	7 ± 2	21 ± 2
Fe35Mn-20Ak	**3**	23 ± 6	35 ± 4	1.6 ± 0.3	5 ± 2	0.4 ± 0.2	5 ± 1	9 ± 2	21 ± 4
D21	**4**	12 ± 4	31 ± 3	1.5 ± 0.4	9 ± 3	0.7 ± 0.4	7 ± 2	8 ± 3	30 ± 1
Fe35Mn-30Ak	**5**	12 ± 5	27 ± 3	10 ± 4	12 ± 4	-	8 ± 3	6 ± 1	26 ± 5
D7	**6**	11 ± 3	26 ± 6	9 ± 4	13 ± 6	1.6 ± 0.2	9 ± 3	5 ± 2	26 ± 4
Fe35Mn-30Ak	**7**	7 ± 4	9 ± 4	9 ± 2	14 ± 4	1.4 ± 0.4	9 ± 3	6 ± 1	43 ± 9
D21	**8**	16 ± 8	30 ± 10	6 ± 1	7 ± 2	0.9 ± 0.3	5 ± 2	7 ± 2	26 ± 6

magnetization and magnetic susceptibility, confirming the MRI-compatibility of the composite materials; (iii) sufficient mechanical properties even after 28 d of biodegradation (*i.e.* σ_y = 1.8–8.3 MPa and E = 0.03–0.53 GPa) which mimicked the mechanical properties of human trabecular bone (σ_y = 0.1–30 MPa and E = 0.01–3 GPa [39]); and (*iv*) a functional environment for the adhesion, proliferation, and osteogenic differentiation of preosteoblasts MC3T3-E1. The combined effect of such favorable properties puts the porous composites developed here forward as one of the top-rank AM Fe-based bone substitutes and encourages *in vivo* studies on such biomaterials.

4.1. Extrusion-based 3D printing of the composite scaffolds

Extrusion-based 3D printing is a viable fabrication technique to produce geometrically complex structures suitable for orthopedic applications [40]. Here, we demonstrated the capability of 3D printing to fabricate prototype hip stem and acetabular cup (Fig. 2**d**) in addition to the cylindrical specimens. The success in extrusion-based 3D printing essentially relies on the choice of a binder that possesses suitable viscoelastic properties. We made choice of a binder made of hypromellose for its shear thinning property (**Fig. S1**) to enable the smooth extrusion of the FeMn-Ak-containing inks (Fig. 2). Hypromellose polymers have been utilized for extrusion-based 3D printing of various metal/ceramic-based inks [41,42]. In addition to the binder, the chemical interactions between the powder particles and binder must be considered. For example, the viscosity of the FeMn-Ak ink increased as the akermanite content increased to 30 vol% (**Fig. S1**). Akermanite powder is hydrophilic, meaning that powder particles can tightly adhere to the hypromellose binder. Consequently, a higher 3D printing pressure was required for the Fe35Mn-30Ak ink as compared to the Fe35Mn-20Ak ink. A sufficient powder-to-binder ratio is another important factor to ensure the stability of the extruded struts and enable the fabrication of the scaffolds with a high aspect ratio and minimal shrinkage.

Robust green bodies of the FeMn-Ak scaffolds were successfully constructed during the 3D printing of the metal-ceramic inks (Fig. 2**b-c**). After 3D printing, the green bodies were subjected to debinding at the temperature where the hypromellose binder decomposed (*i.e.*, at 350°C) [17]. Subsequently, the brown bodies were sintered to form the composites. The as-sintered FeMn-Ak composite scaffolds preserved the original macro-pore design with a lay-down pattern of 0°/90° angle (Fig. 2**e**). In addition to the macro-pores, the struts of the composites possessed open micro-pores (Fig. 2**e-f**), which increased the total interconnectivity of the pore networks. The 0°/90° lay-down pattern of porous scaffold architecture has been reported to lead to more bone formation in cranial rat bone defect than the scaffolds with the 0°/60°/120° angle pattern [43]. This is because the 0°/90° scaffold architecture provides a high concave curvature at the intersections between the struts, which has been shown to attract the initiation of tissue growth *in vivo* in sheep tibia defect model [44].

We supplemented Fe with a 35 wt% Mn to ensure the formation of the γ-austenite Fe-Mn phase, thereby ensuring the antiferromagnetic behavior of the *in situ* formed alloy [5]. The inclusion of 20–30 vol% akermanite was aimed to provide bioactive properties. In addition, interfacial bonding between Fe, Mn, and akermanite is of equal importance for obtaining bone-substituting scaffolds with sufficiently high mechanical performance. Sintering (*i.e.*, at 1200°C) facilitated multiple diffusion processes, which was an effective way to engage every component in the multi-material scaffolds, realizing the intended material biofunctionalities.

The occurrence of diffusion was clearly observed in the cross-sectional analyses of the composite scaffolds (Fig. 3). At a high temperature, Mn is known to be volatile. The compact configuration of the as-printed scaffold struts (Fig. 2**b-c**) allowed volatile Mn to diffuse into Fe and the akermanite particles. Overall, the diffusion of Mn into Fe appeared to be homogenous (Fig. 3**a**), resulting in the formation of the γ-austenite Fe-Mn phase in the scaffolds (Fig. 4**a**). Near the interface of the Fe-Mn alloy to the akermanite phase, the mass% value of Mn in the Fe matrix decreased to about 31–32 wt%. This is expected because Mn diffuses into the neighboring bioceramic particles (Fig. 3**b**).

In addition to the diffusion of Mn into Fe and that of Mn into the bioceramic, Fe dispersed into the bioceramic particles. The diffusion of Fe into silicate-based bioceramics has been reported at the interface of both materials, without the formation of new phases [24,45]. In the present composite scaffolds, an intense level of diffusion of Fe into the bioceramic phase was observed (Fig. 3**b**). Fe diffused approximately 3.2 µm deeper into the akermanite phase than what was previously observed in Fe-Ak composite scaffolds [25]. During the formation of the Fe-Mn solid solution, the α-Fe crystal structure (*i.e.*, body-centered cubic) had transformed into a γ-FeMn crystal structure (*i.e.*, face-centered cubic) that provides more atomic packing, hence enabling more Fe diffusion into the bioceramic phase.

In addition to the γ-austenite Fe-Mn phase in the scaffolds (Fig. 4**a**), the diffusion of Fe and Mn into akermanite displaced the locations of Ca, Mg, and O in the lattice structure. Consequently, a mixture of nesosilicate crystalline phases, including kirschsteinite ($Ca(Fe)SiO_4$), glaucochroite ($Ca(Mn)SiO_4$), and monticellite ($Ca(Mg)SiO_4$), was formed (Fig. 4**a**). The XRD peaks of the nesosilicate phases could not be easily distinguished, since these phases have the same crystal structure (*i.e.*, orthorhombic). The presence of these nesosilicate phases could still be beneficial for bone regeneration. The monticellite phase has been reported to stimulate the adhesion and proliferation of osteoblasts [46]. Moreover, the penetration of Fe into akermanite tends to enhance the apatite-forming ability of the material [47]. Finally, Mn-doped calcium silicate is reported to promote bone regeneration *in vivo* [48].

4.2. Magnetic characteristics of the composite scaffolds

To have MRI compatibility of the first kind, the magnetic susceptibility value of a bone-substituting material under the

hydrated condition must be $< 10^{-2}$ [49]. The magnetic susceptibility values of the porous composites were 3.6 and 4.5 $\times 10^{-3}$ before and after *in vitro* biodegradation, respectively, confirming that the developed biomaterials are paramagnetic and MRI-friendly. The γ-austenite Fe-Mn phase formed during sintering guaranteed the anti-ferromagnetic property of the composite scaffolds (Fig. 4) [50]. The magnetic properties of the scaffolds were comparable to the values found in the literature [6,12,17,50]. Our results showed that the FeMn-Ak composites fall into the same category of magnetic compatibility as Ti6Al4V and non-magnetic stainless steel [49]. While such materials do not react strongly to the applied magnetic field of MRI (*i.e.*, at 2 T), some MRI image artefacts may be present. Such image interference is almost inevitable for most paramagnetic implantable medical devices during MRI imaging. This is due to the huge differences between the magnetic susceptibility of the paramagnetic medical devices (*i.e.*, magnetic susceptibility values of 10^{-5}–10^{-2}) and the surrounding tissue that is mostly diamagnetic (*e.g.*, magnetic susceptibility value -9 $\times$ 10^{-6}) [49,51]. Nonetheless, the volume of MRI image artefacts can be reduced by introducing a porous geometry design into the implant material [52].

4.3. Biodegradation behavior of the composite scaffolds

The FeMn-Ak composite scaffolds biodegraded at the rates of 0.24–0.27 mm/y that are within the suggested range of biodegradation rates suitable for ideal bone substitutes (*i.e.*, 0.2–0.5 mm/y [19]). The biodegradation rates of the composite scaffolds are, indeed, much higher than those of pure Fe [31], Fe-Mn alloys [17], and Fe-Ak composites [25] previously fabricated by extrusion-based 3D printing, and are comparable to those of porous Fe30Mn-hydroxyapatite fabricated by applying the space holder technique [23]. The enhanced biodegradability of the materials is mainly due to the *in situ* alloying of Mn and Fe and the addition of akermanite powder particles. In addition, the composite scaffolds had a high pore interconnectivity that provided a large surface area for the initiation of biodegradation.

The γ-FeMn phase in the composite scaffolds lowers their standard electrode potential, thus increasing their tendency to corrode [12]. The nesosilicate phases formed in the composite scaffolds also influenced the biodegradation behavior. In general, silicate-based bioceramics are known for their favorable biodegradability [53]. Monticellite has a similar solubility to diopside [54], while the solubilities of the kirschsteinite and glaucochroite phases in the physiological condition are yet to be investigated. In the scaffold struts, the nesosilicates particles were randomly distributed and decorated the surfaces of Fe-Mn alloy particles (Fig. 2**f**). The bonding of the materials with multi-phases (*i.e.*, γ-FeMn and nesosilicate phases) may promote local galvanic corrosion, which was, indeed, observed on the cross section of the biodegraded specimens. The Fe-Mn alloy particles exhibited typical pitting corrosion characteristics on their surface (as indicated by arrows in Fig. 5**i**).

During biodegradation, Fe, Mn, Ca, Si, and Mg ions were released from the composite scaffolds (Fig. 6). The ions reacted with the components in the r-SBF medium and formed precipitates (Fig. 5). The biodegradation precipitates on the composite scaffolds were predominantly made of lepidocrocite (γ-FeOOH) and rhodochrosite ($MnCO_3$, Fig. 4**b**). These degradation by-products are expected, as Fe and Mn are the two main constituents in the material composition of the scaffolds. The γ-FeOOH and $MnCO_3$ degradation products are identified in other studies on Fe-Mn alloys as well [55–57]. Despite the formation of Fe- and Mn-based precipitates (Fig. 5), the increasing concentration of Fe^{2+} ions over time and the high concentration of Mn^{2+} ions in the medium collected over the 28 days of immersion showed the continuous biodegradability of the specimens (Fig. 6**a-b**). The concentration of Mn^{2+} ions reached values up to 30 times higher than that of Fe^{2+} ions after only 1 day of immersion. The values remained up to 13 times higher by day 28 (Fig. 6**b**), similar to the trend observed in the biodegradation of FeMn alloys [17]. The higher concentration of Mn^{2+} ions as compared to Fe^{2+} ions implies that the precipitation of Fe-based biodegradation products was favored (Fig. 4**b**). Such excessive release of Mn^{2+} ions has also been reported in previous studies and is strongly correlated to the 5% CO_2 atmospheric condition and the availability of bicarbonate ions (HCO_3^-) in the biodegradation medium [55,56].

The Ca-based precipitates were detected on the periphery of the composite scaffolds with 2–5 wt% calcium concentrations at the measuring points (Fig. 5**f-h**). Unlike Fe-Ak composite scaffolds [25], however, crystalline Ca-based products were not identified. This may be because the concentration of the Ca^{2+} ions released from the nesosilicate phases in the FeMn-Ak scaffolds has been inadequate to form a stable $CaCO_3$ phase (Fig. 6**c**). Moreover, the release of Mn^{2+} ions was substantial throughout the immersion period (Fig. 6**b**). The precipitation of the $MnCO_3$ phase has, therefore, been thermodynamically more favorable than the $CaCO_3$ phase [58]. Despite the absence of crystalline Ca-based precipitates, the Ca^{2+} and PO_4^{3-} ions in the r-SBF medium decreased over time (Fig. 6**c-d**), which suggested the potential formation of amorphous calcium phosphate or calcium carbonate, as biodegradation occurred in the 5% CO_2 environment. The amorphous Ca-based degradation products have been reported to be beneficial for the regeneration of bone tissue [59–61].

Mg- and Si-containing biodegradation products were not observed on the periphery of the biodegradation products (Fig. 5**f-h**). That is because the concentrations of the Mg^{2+} and Si^{4+} ions released from the FeMn-Ak specimens on day 28 (Fig. 6**e-f**) were, respectively, 2 and 6 times lower than those reported during the biodegradation of Fe-Ak composite scaffolds [25]. Our results imply that the nesosilicate bioceramic phases are more stable than pure akermanite, which is in line with the literature [47,48]. When Fe^{3+} had partially substituted the crystal lattice of akermanite, the release of Ca^{2+}, Mg^{2+}, and Si^{4+} ions during biodegradation was lower than the values reported for pure akermanite [47]. A decreasing ion release profile was also reported, when Mn^{2+} diffused into calcium silicate [48]. Nevertheless, the slower dissolution of the nesosilicate phases means that the bioceramic particles could stay longer in the γ-FeMn matrix (Fig. 5**i**) and provide silica-rich surfaces that act as nucleation sites for apatite formation [53], encouraging osteoconductivity.

The observed biodegradation behavior from the immersion tests is intimately linked to the electrochemical response of the composite scaffolds over time. The decreasing OCP values during the immersion tests (Fig. 7**a**) over a total period of 28 days indicate that the base material of the FeMn-Ak composites was increasingly susceptible to corrosion, despite the thickening of the biodegradation products. It implies that biodegradation precipitates moderately limited the mass transport of the material during corrosion, which could be recognized from the decreases in biodegradation rate (Fig. 4**b**) and the marginal increases in R_p value over time (Fig. 7**b**). The impedance modulus values in the low frequency region, which are indicative of the corrosion resistance of the material [62,63], exhibited a stabilizing-to-slight-increasing trend similar to the ones seen for the R_p values (Fig. 7**c-d**). Furthermore, the values of the Bode impedance modulus in the mid-frequency region, which are indicative of the evolution of the corrosion products [62,63], were relatively stable over time. The peaks of the phase angle in the Bode plots did not shift from a higher frequency to a lower frequency when exposed to r-SBF for 28 d (Fig. 7**c-d**), which suggests that the partial growth and dissolution of the corrosion products was near equivalent. Corresponding to the trend of OCP values, the peaks of the phase angle in the Bode plots at high frequencies (*e.g.*, 10 kHz) remained close to 0°, indicating that

the material had a propensity to corrode [64,65]. Altogether, our results demonstrated that the rate and mechanism of biodegradation of the composite scaffolds developed here, as well as the associated biodegradation products, supported their intended use as temporary bone substitutes.

4.4. Mechanical properties of the composite scaffolds

The structural integrity of biodegradable implants is of importance and should be maintained until newly formed bone takes over the role of mechanical support. As compared to geometrically similar scaffolds made from the Fe35Mn alloy [17] (*i.e.*, $\phi = 10.16$ mm, $h = 10.55$ mm, a lay-down pattern design of 0°/90° angle, a strut size of 412 µm and a porosity of 69%), the Fe35Mn-20Ak composite scaffolds developed here exhibited a higher yield strength and elastic modulus. However, the Fe35Mn-30Ak composite scaffolds exhibited lower mechanical properties than the Fe35Mn alloy scaffolds [17]. Increasing the content of the reinforcing akermanite particles from 20 to 30 vol% decreased the yield strength and the elastic modulus of the resulting biomaterial (Fig. 8). This is likely due to the embrittlement effect of the bioceramic phase on the metal matrix [66–68]. Nevertheless, both the FeMn-Ak composite scaffolds developed in this study (*i.e.*, $\sigma_y = 3.1$–8.3 MPa and $E = 0.03$–0.5 GPa) exhibited trabecular bone-mimicking mechanical properties ($\sigma_y = 0.1$–30 MPa and $E = 0.01$–3 GPa [39]) even after 28 d of biodegradation.

For any scaffolds containing multiple material components, strong bonding at the interface of the components is required to ensure smooth load transfer from the matrix to the reinforcing phases so as to prevent premature failure of the composite material as a whole. On the other hand, the interfacial bonding of the phases can act as the initiation sites for localized corrosion, which may adversely influence the mechanical integrity of the composite material during biodegradation. In the FeMn-Ak composites, the diffusion of Fe and Mn into the bioceramic phase was clearly observed along with the formed Fe-,Mn-containing bioceramic phases (Figs. 3**,** 4**a**). The diffusion resulted in strong bonding of the multi-material phases, thus leading to the higher yield strength and elastic modulus of the Fe35Mn-20Ak scaffolds as compared to those of the Fe-20Ak specimens [25].

During biodegradation, the mechanical properties of the FeMn-20Ak specimens decreased with time, as has been the case for Fe-Ak [25] and Fe-TCP [69] composites. The Fe35Mn-30Ak specimens turned brittle and did not exhibit the typical elastic-plastic deformation behavior after 14 and 28 d *in vitro* biodegradation. Given the deteriorating effects of 28 d of biodegradation and the negligible strengthening effects of the precipitated degradation products, the mechanical properties of the Fe35Mn-30Ak scaffolds were expected to decrease. It should, however, be noted that these composite scaffolds did not fail prematurely, but at a quite large strain value of >10% under uniaxial compression.

4.5. Cytocompatibility and osteogenic potential of the composite scaffolds

In the development of osteoregenerative biodegradable materials, osteogenic responses are of importance. The FeMn-Ak composite scaffolds developed here proved to be non-cytotoxic for MC3T3-E1 cells (Fig. 9**a-b**) and while biodegrading, they supported the adhesion, proliferation and extracellular matrix formation over the 21 d of cell culture (Fig. 9**c-f**). In addition, the precipitated minerals, which could be a combination of biodegradation products and apatite, integrated well into the cellular matrix (Fig. 9**e-f**, Table 2). The composite scaffolds also enabled the osteogenic differentiation of the cells, as evidenced by the expression of Runx2 and at the later time points, the presence of OPN in the extracellular matrix of the cells was observed (Fig. 9**g-h**).

Initially, we assessed the metabolic activity of the MC3T3-E1 preosteoblasts cultured with the extracts of the composite specimens. The inhibition of the preosteoblasts growth (IC_{50}) has been reported at 53 mg/L Fe ions and 5 mg/L Mn ions [70]. We observed that the preosteoblasts metabolic activity declined in the extracts of the composite scaffolds with high concentrations (Fig. 9**a-b**). In the 100% extracts, the concentration of Fe^{2+} ions alone would be high enough to inhibit the metabolic activity of the cells. While the concentration of Fe^{2+} ions reduced to a safe value in the 75% extracts, the concentration of Mn^{2+} ions in both extracts remained high enough to adversely affect cell activity, as observed in the 75% Fe35Mn-20Ak extracts (Fig. 9**a**). Interestingly, the high concentration of Mn^{2+} ions in the 75% Fe35Mn-30Ak extracts did not negatively influence the metabolic activity of the preosteoblasts (Fig. 9**b**). This could be due to the presence of a higher concentration of bioactive ions released from the silicate-based ceramics in the Fe35Mn-30Ak specimens. When further diluted (*i.e.*, 2× and more), the preosteoblasts were metabolically active, despite the fact that the concentration of Mn ions (*i.e.*, 15–18 mg/L) was still higher than the reported IC_{50} value. Bone tissue is known to have a large amount of Mn reserve [71], which may explain the non-cytotoxic results for the preosteoblasts in the 50% and 25% FeMn-Ak extracts.

Then, we evaluated the growth of the preosteoblasts directly cultured on the specimens. We used a high ratio of the cell culture medium to the surface area of the specimen in order to more closely mimic the conditions experienced by the specimens in the human body. Our results demonstrated the adhesion and proliferation of cells on both types of the composite scaffolds (Fig. 9**c-f, S5**), which were comparable to one of the currently most widely used biomaterials for permanent bone implants (*i.e.*, Ti6Al4V, **Fig. S6**) and to bioactive Fe-Ak [25]. Importantly, the *in vitro* biological responses of these cells to the composites were improved as compared to the cell responses to the Fe35Mn alloy specimens (**Fig. S7**), and to those observed in our previous studies on geometrically similar Fe [31] and Fe-Mn specimens [17]. These comparisons confirm that the enhanced cytocompatibility of the developed biomaterials is due to the addition of the silicate-based bioceramics to the γ-FeMn matrix. Moreover, the direct cell culture results did not show any noticeable differences in the cell proliferation between the two composite specimen groups, unlike the results from the indirect cell culture. This is most likely because the cells were continuously exposed to the FeMn-Ak extracts in the indirect cell tests, while the cells received a fresh cell culture medium in the direct cell tests. The metallic ions, therefore, did not accumulate to cause cytotoxicity.

The improved cytocompatibility of the FeMn-based composites due to the addition of silicate-based bioceramic is obviously due to the release of bioactive ions, most notably Ca^{2+}, Mg^{2+} and Si^{4+} ions that have been reported to be involved in many mechanisms and pathways of bone cell growth and differentiation. For the mineralization process to occur, bone cells have to absorb Ca^{2+} and PO_4^{3-} ions, and synthesize extracellular matrix (*e.g.*, type I collagen or OPN [72]). The absorbed Ca/P minerals are then transported to the extracellular space to precipitate, nucleate, and crystallize on the matrix into bony apatite. The availability of ample Ca ions is one of the keys to ensuring successful apatite mineralization [73]. Moreover, Si ions have been shown to be involved in the wingless-related integration (Wnt) and sonic hedgehog homolog (SHH) signaling pathway [27] as well as Wnt/β-catenin pathways [74] that are directly related to the osteogenic differentiation mechanism. Besides that, Mg ions at concentrations ranging from 2 to 10 mm have been reported to improve cell proliferation and osteogenic activity by increasing calcitonin gene-related polypeptide-α (CGRP)

to induce cAMP responsive element binding protein 1 (CREB1) and Osterix (or Sp7) expression and to be involved in various signaling pathways, such as in transient receptor potential cation channel subfamily M member 7 (TRPM7) channels that regulate Mg ions to promote osteoinduction *via* the phosphoinositide-3-kinase–protein kinase (PI3K) pathway, or in mitogen-activated protein kinase (MAPK)/extracellular signal-regulated kinase (ERK) and Wnt/β-catenin pathways that are closely related to bone formation [26]. In agreement with the literature, we have demonstrated the FeMn-Ak composite scaffolds allowed for the differentiation of preosteoblasts, as revealed by Runx2 expression, the extracellular matrix OPN (Fig. 9**g-h**), and the detection of precipitates containing Ca and P fully integrated into the extracellular matrix (Fig. 9**e-f,** Table 2). Overall, the *in vitro* biological performance of FeMn-Ak composite specimens was superior to the FeMn alloy scaffolds [17] and comparable to that of the Fe-Ak composites [25], despite that akermanite in the FeMn-Ak specimens was transformed into nesosilicate crystalline phases. Taken together, our findings demonstrate the potential of the developed 3D printed FeMn-Ak porous biomaterials to be used as biodegradable, MRI-friendly and osteogenic Fe-based bone substitutes.

5. Conclusions

We developed two types of bone-substituting 3D printed biodegradable FeMn-akermanite composite scaffolds. Our thorough characterization of these biomaterials showed that they offer suitable rates of biodegradability, are MRI-friendly and osteogenic, and mimic the trabecular bone in terms of mechanical properties. The porosity and pore interconnectivity of the composites were both high to meet their functional requirements. The *in vitro* biodegradation rates of the composites fell into the range of the desired values for ideal bone substitution. The γ-FeMn phase in the composite made the biomaterials weakly paramagnetic, allowing the composites to be classified as first kind MRI-friendly biomaterials. The mechanical properties of the porous composite remained in the range of those of the trabecular bone, despite the decreasing trend due to *in vitro* biodegradation. The preosteoblast MC3T3-E1 cell line showed a positive *in vitro* biological response to the composite materials, as evidenced by the adhesion, proliferation, and differentiation of the cells. Altogether, our results evidently show the remarkable potential of the FeMn-Ak composites in fulfilling the requirements of porous biodegradable bone substitutes, encouraging further research towards their clinical translation.

Data availability statement

Data will be made available on request.

Declaration of Competing Interest

The authors declare that they have no known competing financial interests or personal relationships that could have appeared to influence the work reported in this paper.

CRediT authorship contribution statement

N.E. Putra: Conceptualization, Methodology, Investigation, Validation, Writing – original draft, Visualization. **M.A. Leeflang:** Methodology, Investigation. **M. Klimopoulou:** Methodology, Investigation. **J. Dong:** Investigation. **P. Taheri:** Methodology, Writing – review & editing. **Z. Huan:** Resources, Writing – review & editing. **L.E. Fratila-Apachitei:** Resources, Supervision, Writing – review & editing. **J.M.C. Mol:** Resources, Supervision, Writing – review & editing. **J. Chang:** Resources, Writing – review & editing. **J. Zhou:** Conceptualization, Resources, Supervision, Writing – review & editing. **A.A. Zadpoor:** Conceptualization, Resources, Supervision, Funding acquisition, Writing – review & editing.

Acknowledgments

This work is part of the 3DMed project that received the funding from the Interreg 2 Seas program 2014 – 2020, co-funded by the European Regional Development Fund under subsidy contract No. 2S04-014. J. Dong thank the China Scholarship Council (CSC) for financial support. The authors acknowledged Mr. Ruud Hendrikx at the Department of Materials Science and Engineering, Delft University of Technology for XRD analysis. The authors thank Mrs. Agnieszka Kooijman at the Department of Materials Science and Engineering, Delft University of Technology for her assistance in electrochemical experiments. The authors acknowledged Mr. Michel van den Brink at the Department of Process and Energy, Delft University of Technology for ICP-OES analysis.

Supplementary materials

Supplementary material associated with this article can be found, in the online version, at doi:10.1016/j.actbio.2023.03.033.

References

[1] A.H. Md Yusop, M.F. Ulum, A. Al Sakkaf, D. Hartanto, H. Nur, Insight into the bioabsorption of Fe-based materials and their current developments in bone applications, Biotechnol. J. 16 (2021), doi:10.1002/biot.202100255.
[2] R. Gorejová, L. Haverová, R. Oriňaková, A. Oriňak, M. Oriňak, Recent advancements in Fe-based biodegradable materials for bone repair, J. Mater. Sci. 54 (2019) 1913–1947, doi:10.1007/s10853-018-3011-z.
[3] A.H. Md Yusop, A. Al Sakkaf, H. Nur, Modifications on porous absorbable Fe-based scaffolds for bone applications: a review from corrosion and biocompatibility viewpoints, J. Biomed. Mater. Res. - Part B Appl. Biomater. 110 (2022) 18–44, doi:10.1002/jbm.b.34893.
[4] Y. Li, H. Jahr, P. Pavanram, F.S.L. Bobbert, U. Puggi, X.Y. Zhang, B. Pouran, M.A. Leeflang, H. Weinans, J. Zhou, A.A. Zadpoor, Additively manufactured functionally graded biodegradable porous iron, Acta Biomater. 96 (2019) 646–661, doi:10.1016/j.actbio.2019.07.013.
[5] J. Martínez, S.M. Cotes, A.F. Cabrera, J. Desimoni, A. Fernández Guillermet, On the relative fraction of ε martensite in γ-Fe-Mn alloys, Mater. Sci. Eng. A 408 (2005) 26–32, doi:10.1016/j.msea.2005.06.019.
[6] Y.P. Feng, A. Blanquer, J. Fornell, H. Zhang, P. Solsona, M.D. Baró, S. Suriñach, E. Ibáñez, E. García-Lecina, X. Wei, R. Li, L. Barrios, E. Pellicer, C. Nogués, J. Sort, Novel Fe-Mn-Si-Pd alloys: insights into mechanical, magnetic, corrosion resistance and biocompatibility performances, J. Mater. Chem. B 4 (2016) 6402–6412, doi:10.1039/c6tb01951j.
[7] S.M. Huang, E.A. Nauman, L.A. Stanciu, Investigation of porosity on mechanical properties, degradation and *in-vitro* cytotoxicity limit of Fe30Mn using space holder technique, Mater. Sci. Eng. C 99 (2019) 1048–1057, doi:10.1016/j.msec.2019.02.055.
[8] P. Liu, D. Zhang, Y. Dai, J. Lin, Y. Li, C. Wen, Microstructure, mechanical properties, degradation behavior, and biocompatibility of porous Fe-Mn alloys fabricated by sponge impregnation and sintering techniques, Acta Biomater. 114 (2020) 485–496, doi:10.1016/j.actbio.2020.07.048.
[9] C. Shuai, W. Yang, Y. Yang, H. Pan, C. He, F. Qi, D. Xie, H. Liang, Selective laser melted Fe-Mn bone scaffold: microstructure, corrosion behavior and cell response, Mater. Res. Express. 7 (2019) 015404, doi:10.1088/2053-1591/ab62f5.
[10] D. Carluccio, C. Xu, J. Venezuela, Y. Cao, D. Kent, M. Bermingham, A.G. Demir, B. Previtali, Q. Ye, M. Dargusch, Additively manufactured iron-manganese for biodegradable porous load-bearing bone scaffold applications, Acta Biomater. 103 (2020) 346–360, doi:10.1016/j.actbio.2019.12.018.
[11] Y. Nie, G. Chen, H. Peng, S. Tang, Z. Zhou, F. Pei, B. Shen, *In vitro* and 48 weeks *in vivo* performances of 3D printed porous Fe-30Mn biodegradable scaffolds, Acta Biomater. 121 (2021) 724–740, doi:10.1016/j.actbio.2020.12.028.
[12] M.S. Dargusch, A. Dehghan-Manshadi, M. Shahbazi, J. Venezuela, X. Tran, J. Song, N. Liu, C. Xu, Q. Ye, C. Wen, Exploring the role of manganese on the microstructure, mechanical properties, biodegradability, and biocompatibility of porous iron-based scaffolds, ACS Biomater. Sci. Eng. 5 (2019) 1686–1702, doi:10.1021/acsbiomaterials.8b01497.
[13] D. Hong, D.T. Chou, O.I. Velikokhatnyi, A. Roy, B. Lee, I. Swink, I. Issaev, H.A. Kuhn, P.N. Kumta, Binder-jetting 3D printing and alloy development of new biodegradable Fe-Mn-Ca/Mg alloys, Acta Biomater. 45 (2016) 375–386, doi:10.1016/j.actbio.2016.08.032.
[14] D.T. Chou, D. Wells, D. Hong, B. Lee, H. Kuhn, P.N. Kumta, Novel processing of iron-manganese alloy-based biomaterials by inkjet 3-D printing, Acta Biomater. 9 (2013) 8593–8603, doi:10.1016/j.actbio.2013.04.016.
[15] H. Hermawan, A. Purnama, D. Dube, J. Couet, D. Mantovani, Fe-Mn alloys for metallic biodegradable stents: degradation and cell viability studies, Acta Biomater. 6 (2010) 1852–1860, doi:10.1016/j.actbio.2009.11.025.

[16] J. Čapek, J. Kubásek, D. Vojtěch, E. Jablonská, J. Lipov, T. Ruml, Microstructural, mechanical, corrosion and cytotoxicity characterization of the hot forged FeMn30(wt.%) alloy, Mater. Sci. Eng. C 58 (2016) 900–908, doi:10.1016/j.msec.2015.09.049.

[17] N.E. Putra, M.A. Leeflang, P. Taheri, L.E. Fratila-Apachitei, J.M.C. Mol, J. Zhou, A.A. Zadpoor, Extrusion-based 3D printing of *ex situ*-alloyed highly biodegradable MRI-friendly porous iron-manganese scaffolds, Acta Biomater. 134 (2021) 774–790, doi:10.1016/j.actbio.2021.07.042.

[18] J. Venezuela, M.S. Dargusch, Addressing the slow corrosion rate of biodegradable Fe-Mn: current approaches and future trends, Curr. Opin. Solid State Mater. Sci. 24 (2020) 100822, doi:10.1016/j.cossms.2020.100822.

[19] C. Shuai, S. Li, S. Peng, P. Feng, Y. Lai, C. Gao, Biodegradable metallic bone implants, Mater. Chem. Front. 3 (2019) 544–562, doi:10.1039/c8qm00507a.

[20] B. Huzum, B. Puha, R. Necoara, S. Gheorghevici, G. Puha, A. Filip, P. Sirbu, O. Alexa, Biocompatibility assessment of biomaterials used in orthopedic devices: an overview (Review), Exp. Ther. Med 22 (2021) 1–9, doi:10.3892/etm.2021.10750.

[21] S. Mandal, V. Kishore, M. Bose, S.K. Nandi, M. Roy, In vitro and in vivo degradability, biocompatibility and antimicrobial characteristics of Cu added iron-manganese alloy, J. Mater. Sci. Technol. 84 (2021) 159–172, doi:10.1016/j.jmst.2020.12.029.

[22] L.C. Trincă, L. Burtan, D. Mareci, B.M. Fernández-Pérez, I. Stoleriu, T. Stanciu, S. Stanciu, C. Solcan, J. Izquierdo, R.M. Souto, Evaluation of *in vitro* corrosion resistance and *in vivo* osseointegration properties of a FeMnSiCa alloy as potential degradable implant biomaterial, Mater. Sci. Eng. C 118 (2021) 111436, doi:10.1016/j.msec.2020.111436.

[23] M. Heiden, E. Nauman, L. Stanciu, Bioresorbable Fe–Mn and Fe–Mn–HA materials for orthopedic implantation: enhancing degradation through porosity control, Adv. Healthc. Mater. 6 (2017) 1–12, doi:10.1002/adhm.201700120.

[24] C. Shuai, Y. Li, Y. Yang, S. Peng, W. Yang, F. Qi, S. Xiong, H. Liang, L. Shen, Bioceramic enhances the degradation and bioactivity of iron bone implant, Mater. Res. Express. 6 (2019) 115401, doi:10.1088/2053-1591/ab45b9.

[25] N.E. Putra, K.G.N. Borg, P.J. Diaz-Payno, M.A. Leeflang, M. Klimopoulou, P. Taheri, J.M.C. Mol, L.E. Fratila-Apachitei, Z. Huan, J. Chang, J. Zhou, A.A. Zadpoor, Additive manufacturing of bioactive and biodegradable porous iron-akermanite composites for bone regeneration, Acta Biomater. 148 (2022) 355–373, doi:10.1016/j.actbio.2022.06.009.

[26] Z. Yuan, Z. Wan, C. Gao, Y. Wang, J. Huang, Q. Cai, Controlled magnesium ion delivery system for *in situ* bone tissue engineering, J. Control. Release. 350 (2022) 360–376, doi:10.1016/j.jconrel.2022.08.036.

[27] P. Han, C. Wu, Y. Xiao, The effect of silicate ions on proliferation, osteogenic differentiation and cell signalling pathways (WNT and SHH) of bone marrow stromal cells, Biomater. Sci. 1 (2013) 379–392, doi:10.1039/c2bm00108j.

[28] N.E. Putra, M.J. Mirzaali, I. Apachitei, J. Zhou, A.A. Zadpoor, Multi-material additive manufacturing technologies for Ti-, Mg-, and Fe-based biomaterials for bone substitution, Acta Biomater. 109 (2020) 1–20, doi:10.1016/j.actbio.2020.03.037.

[29] C. Wu, J. Chang, Synthesis and apatite-formation ability of akermanite, Mater. Lett. 58 (2004) 2415–2417, doi:10.1016/j.matlet.2004.02.039.

[30] ASTM B963-17, Standard test methods for oil content, oil-impregnation efficiency, and surface-connected porosity of sintered powder metallurgy (PM) products using Archimedes' principle, ASTM International, 2017. 10.1520/B0963-14.

[31] N.E. Putra, M.A. Leeflang, M. Minneboo, P. Taheri, L.E. Fratila-Apachitei, J.M.C. Mol, J. Zhou, A.A. Zadpoor, Extrusion-based 3D printed biodegradable porous iron, Acta Biomater. 121 (2021) 741–756, doi:10.1016/j.actbio.2020.11.022.

[32] A. Oyane, H.M. Kim, T. Furuya, T. Kokubo, T. Miyazaki, T. Nakamura, Preparation and assessment of revised simulated body fluids, J. Biomed. Mater. Res. - Part A 65 (2003) 188–195, doi:10.1002/jbm.a.10482.

[33] L. Yang, E. Zhang, Biocorrosion behavior of magnesium alloy in different simulated fluids for biomedical application, Mater. Sci. Eng. C 29 (2009) 1691–1696, doi:10.1016/j.msec.2009.01.014.

[34] ASTM G1-03, Standard practice for preparing, cleaning, and evaluating corrosion test specimens, ASTM Int. (2017), doi:10.1520/G0001-03R17E01.2.

[35] ASTM G32-72, Standard practice for laboratory immersion corrosion testing of metals, ASTM Int. (2004), doi:10.1520/G0031-72R04.2.

[36] ISO 13314, Mechanical testing of metals - Ductility testing - compression test for porous and cellular metals, Int. Organ. Stand. (2011) https://www.iso.org.

[37] ISO 10993-12, Biological evaluation of medical devices - Part 12: Sample preparation and reference materials, 2012.

[38] ISO 10993-5Tests for *in vitro* cytotoxicity, International Organization for Standardization, 2009, doi:10.1021/es0620181.

[39] E.F. Morgan, G.U. Unnikrisnan, A.I. Hussein, Bone mechanical properties in healthy and diseased states, Annu. Rev. Biomed. Eng. 20 (2018) 119–143, doi:10.1146/annurev-bioeng-062117-121139.

[40] J.P. Li, P. Habibovic, M. van den Doel, C.E. Wilson, J.R. de Wijn, C.A. van Blitterswijk, K. de Groot, Bone ingrowth in porous titanium implants produced by 3D fiber deposition, Biomaterials 28 (2007) 2810–2820, doi:10.1016/j.biomaterials.2007.02.020.

[41] M.W. Sa, B.N.B. Nguyen, R.A. Moriarty, T. Kamalitdinov, J.P. Fisher, J.Y. Kim, Fabrication and evaluation of 3D printed BCP scaffolds reinforced with ZrO2 for bone tissue applications, Biotechnol. Bioeng. 115 (2018) 989–999, doi:10.1002/bit.26514.

[42] C.F. Marques, F.H. Perera, A. Marote, S. Ferreira, S.I. Vieira, S. Olhero, P. Miranda, J.M.F. Ferreira, Biphasic calcium phosphate scaffolds fabricated by direct write assembly: mechanical, anti-microbial and osteoblastic properties, J. Eur. Ceram. Soc. 37 (2017) 359–368, doi:10.1016/j.jeurceramsoc.2016.08.018.

[43] A. Berner, M.A. Woodruff, C.X.F. Lam, M.T. Arafat, S. Saifzadeh, R. Steck, J. Ren, M. Nerlich, A.K. Ekaputra, I. Gibson, D.W. Hutmacher, Effects of scaffold architecture on cranial bone healing, Int. J. Oral Maxillofac. Surg. 43 (2014) 506–513, doi:10.1016/j.ijom.2013.05.008.

[44] M. Paris, A. Götz, I. Hettrich, C.M. Bidan, J.W.C. Dunlop, H. Razi, I. Zizak, D.W. Hutmacher, P. Fratzl, G.N. Duda, W. Wagermaier, A. Cipitria, Scaffold curvature-mediated novel biomineralization process originates a continuous soft tissue-to-bone interface, Acta Biomater. 60 (2017) 64–80, doi:10.1016/j.actbio.2017.07.029.

[45] H. Ma, T. Li, Z. Huan, M. Zhang, Z. Yang, J. Wang, J. Chang, C. Wu, 3D printing of high-strength bioscaffolds for the synergistic treatment of bone cancer, NPG Asia Mater. 10 (2018) 31–44, doi:10.1038/s41427-018-0015-8.

[46] X. Chen, J. Ou, Y. Kang, Z. Huang, H. Zhu, G. Yin, H. Wen, Synthesis and characteristics of monticellite bioactive ceramic, J. Mater. Sci. Mater. Med. 19 (2008) 1257–1263, doi:10.1007/s10856-007-3233-0.

[47] M. Myat-Htun, A.F. Mohd Noor, M. Kawashita, Y.M. Baba Ismail, Tailoring mechanical and *in vitro* biological properties of calcium–silicate based bioceramic through iron doping in developing future material, J. Mech. Behav. Biomed. Mater. 128 (2022) 105122, doi:10.1016/j.jmbbm.2022.105122.

[48] Z. Du, H. Leng, L. Guo, Y. Huang, T. Zheng, Z. Zhao, X. Liu, X. Zhang, Q. Cai, X. Yang, Calcium silicate scaffolds promoting bone regeneration via the doping of Mg2+ or Mn2+ ion, Compos. Part B Eng. 190 (2020) 107937, doi:10.1016/j.compositesb.2020.107937.

[49] J.F. Schenck, The role of magnetic susceptibility in magnetic resonance imaging: MRI magnetic compatibility of the first and second kinds, Med. Phys. 23 (1996) 815–850, doi:10.1118/1.597854.

[50] H. Hermawan, D. Dubé, D. Mantovani, Degradable metallic biomaterials: design and development of Fe-Mn alloys for stents, J. Biomed. Mater. Res. - Part A 93 (2010) 1–11, doi:10.1002/jbm.a.32224.

[51] P.M. Jungmann, C.A. Agten, C.W. Pfirrmann, R. Sutter, Advances in MRI around metal, J. Magn. Reson. Imaging 46 (2017) 972–991, doi:10.1002/jmri.25708.

[52] L.N. Carter, O. Addison, N. Naji, P. Seres, A.H. Wilman, D.E.T. Shepherd, L. Grover, S. Cox, Reducing MRI susceptibility artefacts in implants using additively manufactured porous Ti-6Al-4V structures, Acta Biomater. 107 (2020) 338–348, doi:10.1016/j.actbio.2020.02.038.

[53] P. Srinath, P. Abdul Azeem, K. Venugopal Reddy, Review on calcium silicate-based bioceramics in bone tissue engineering, Int. J. Appl. Ceram. Technol. 17 (2020) 2450–2464, doi:10.1111/ijac.13577.

[54] S.K. Venkatraman, R. Choudhary, G. Krishnamurithy, H.R. Balaji Raghavendran, M.R. Murali, T. Kamarul, A. Suresh, J. Abraham, S. Praharaj, S. Swamiappan, Comparative investigation on antibacterial, biological and mechanical behaviour of monticellite and diopside derived from biowaste for bone regeneration, Mater. Chem. Phys. 286 (2022) 126157, doi:10.1016/j.matchemphys.2022.126157.

[55] E. Mouzou, C. Paternoster, R. Tolouei, A. Purnama, P. Chevallier, D. Dubé, F. Prima, D. Mantovani, In vitro degradation behavior of Fe-20Mn-1.2C alloy in three different pseudo-physiological solutions, Mater. Sci. Eng. C 61 (2016) 564–573, doi:10.1016/j.msec.2015.12.092.

[56] S. Gambaro, C. Paternoster, B. Occhionero, J. Fiocchi, C.A. Biffi, A. Tuissi, D. Mantovani, Mechanical and degradation behavior of three Fe-Mn-C alloys for potential biomedical applications, Mater. Today Commun. 27 (2021) 102250, doi:10.1016/j.mtcomm.2021.102250.

[57] E. Mouzou, C. Paternoster, R. Tolouei, P. Chevallier, C.A. Biffi, A. Tuissi, D. Mantovani, CO2-rich atmosphere strongly affects the degradation of Fe-21Mn-1C for biodegradable metallic implants, Mater. Lett. 181 (2016) 362–366, doi:10.1016/j.matlet.2016.06.017.

[58] J.G. Speight, Lange's Handbook of Chemistry, McGraw-hill, New York, 2005.

[59] X. Wang, M. Ackermann, S. Wang, E. Tolba, M. Neufurth, Q. Feng, H.C. Schröder, W.E.G. Müller, Amorphous polyphosphate/amorphous calcium carbonate implant material with enhanced bone healing efficacy in a critical-size defect in rats, Biomed. Mater. 11 (2016), doi:10.1088/1748-6041/11/3/035005.

[60] W.E.G. Müller, M. Neufurth, S. Wang, M. Ackermann, R. Muñoz-Espí, Q. Feng, Q. Lu, H.C. Schröder, X. Wang, Amorphous, smart, and bioinspired polyphosphate nano/microparticles: a biomaterial for regeneration and repair of osteo-articular impairments in-situ, Int. J. Mol. Sci. 19 (2018), doi:10.3390/ijms19020427.

[61] E. Tolba, W.E.G. Müller, B.M. Abd El-Hady, M. Neufurth, F. Wurm, S. Wang, H.C. Schröder, X. Wang, High biocompatibility and improved osteogenic potential of amorphous calcium carbonate/vaterite, J. Mater. Chem. B 4 (2016) 376–386, doi:10.1039/c5tb02228b.

[62] J. Tedim, M.L. Zheludkevich, A.C. Bastos, A.N. Salak, A.D. Lisenkov, M.G.S. Ferreira, Influence of preparation conditions of layered double hydroxide conversion films on corrosion protection, Electrochim. Acta 117 (2014) 164–171, doi:10.1016/j.electacta.2013.11.111.

[63] B. Van der Linden, H. Terryn, J. Vereecken, Investigation of anodic aluminium oxide layers by electrochemical impedance spectroscopy, J. Appl. Electrochem. 20 (1990) 798–803, doi:10.1007/BF01094309.

[64] M. Mahdavian, M.M. Attar, Another approach in analysis of paint coatings with EIS measurement: phase angle at high frequencies, Corros. Sci. 48 (2006) 4152–4157, doi:10.1016/j.corsci.2006.03.012.

[65] Y. Zuo, R. Pang, W. Li, J.P. Xiong, Y.M. Tang, The evaluation of coating performance by the variations of phase angles in middle and high frequency domains of EIS, Corros. Sci. 50 (2008) 3322–3328, doi:10.1016/j.corsci.2008.08.049.

[66] M. Dehestani, E. Adolfsson, L.A. Stanciu, Mechanical properties and corrosion behavior of powder metallurgy iron-hydroxyapatite composites for biodegradable implant applications, Mater. Des. 109 (2016) 556–569, doi:10.1016/j.matdes.2016.07.092.
[67] E.B. Montufar, M. Casas-Luna, M. Horynová, S. Tkachenko, Z. Fohlerová, S. Diaz-de-la-Torre, K. Dvořák, L. Čelko, J. Kaiser, High strength, biodegradable and cytocompatible alpha tricalcium phosphate-iron composites for temporal reduction of bone fractures, Acta Biomater. 70 (2018) 293–303, doi:10.1016/j.actbio.2018.02.002.
[68] P. Feng, C. Gao, C. Shuai, S. Peng, Toughening and strengthening mechanisms of porous akermanite scaffolds reinforced with nano-titania, RSC Adv. 5 (2015) 3498–3507, doi:10.1039/c4ra12095g.
[69] A. Reindl, R. Borowsky, S.B. Hein, J. Geis-Gerstorfer, P. Imgrund, F. Petzoldt, Degradation behavior of novel Fe/ß-TCP composites produced by powder injection molding for cortical bone replacement, J. Mater. Sci. 49 (2014) 8234–8243, doi:10.1007/s10853-014-8532-5.
[70] A. Yamamoto, R. Honma, M. Sumita, Cytotoxicity evaluation of 43 metal salts using murine fibroblasts and osteoblastic cells, J. Biomed. Mater. Res. 39 (1998) 331–340. 10.1002/(SICI)1097-4636(199802)39:2⟨331::AID-JBM22⟩3.0.CO;2-E.
[71] P. Chen, J. Bornhorst, M. Aschner, Manganese metabolism in humans, Front. Biosci. - Landmark. 23 (2018) 1655–1679, doi:10.2741/4665.
[72] Z.Y. Qiu, Y. Cui, X.M. Wang, Chapter 1 - Natural bone tissue and its biomimetic, Mineralized collagen Bone Graft Substitutes, Elsevier Ltd, 2019, doi:10.1016/B978-0-08-102717-2.00001-1.
[73] J. Zhang, Y. Ji, S. Jiang, M. Shi, W. Cai, R.J. Miron, Y. Zhang, Calcium-collagen coupling is vital for biomineralization schedule, Adv. Sci. 8 (2021) 1–15, doi:10.1002/advs.202100363.
[74] J. Guan, J. Zhang, S. Guo, H. Zhu, Z. Zhu, H. Li, Y. Wang, C. Zhang, J. Chang, Human urine-derived stem cells can be induced into osteogenic lineage by silicate bioceramics via activation of the Wnt/β-catenin signaling pathway, Biomaterials 55 (2015) 1–11, doi:10.1016/j.biomaterials.2015.03.029.